Bayesian inference of thermodynamic models from vapor flow experiments

Giulio Gori, Marta Zocca, Alberto Guardone, Olivier Le Maitre, Pietro Marco Congedo

Bayesian inference of thermodynamic models from vapor flow experiments

G. Gori[a,*], M. Zocca[b], A. Guardone[b], O.P. Le Maître[c], P.M. Congedo[a]

[a] *INRIA, Centre de Mathématiques Appliquées, École Polytechnique, IPP, Route de Saclay, 91128 Palaiseau, France, giulio.gori@inria.fr and pietro.congedo@inria.fr*

[b] *Department of Aerospace Science & Technology, Politecnico di Milano, Via La Masa 35, 20156 Milano, Italy, martamaria.zocca@polimi.it and alberto.guardone@polimi.it*

[c] *CNRS, Centre de Mathématiques Appliquées, INRIA, École Polytechnique, IPP, Route de Saclay, 91128 Palaiseau, France olivier.le-maitre@polytechnique.edu*

Abstract

The present work concerns the inference of the coefficients of fluid-dependent thermodynamic models, applicable to complex molecular compounds with non-ideal effects. The main objective is to numerically assess the potential of using experimental measurements of some expansion flows to infer the model parameters. The Bayesian formulation incorporates uncertainties in the flow conditions and measurement errors and compares the measurements with the predictions of Computational Fluid Dynamics (CFD) simulations which depend on the parameter values. The resulting parameters posterior distribution is sampled using a Markov-Chain Monte-Carlo method. Polynomial-Chaos (PC) surrogates substitute the CFD predictions in the definition of the Bayesian posterior, in order to alleviate the computational burden of solving multiple CFD problems. We rely on synthetic data *i.e.*, generated numerically, to assess the potential of expansion flow experiments. Using synthetic data prevents experimental bias, enables the control of model errors (thermodynamic and flow models) and permits the measurement of quantities in conditions that would be hardly achievable in practice. We test three expansion flows with increasing non-ideal effects. Our analyses reveal that the considered experiments have limited potential for the inference of the thermodynamic coefficients. Measuring the temperature, in addition to pressure, improves the posterior knowledge of the specific heat ratio, but other parameters remain highly uncertain. Also, the selection of an expansion condition yielding higher non-ideal effects somehow improves the inference, but the trend is limited, and experimenting with these conditions may be challenging. Our work also supports the use of Bayesian analysis with synthetic data to investigate, analyze, and design new experiments in the future.

Keywords: Non-ideal Compressible-Fluid Dynamics, Parameter calibration, Bayesian Inference, MCMC, ORC applications, Siloxane fluid MDM

1. Introduction

Non-Ideal Compressible Fluid Dynamics (NICFD) focuses on the investigation of compressible fluid flows in peculiar thermodynamic conditions. In this regime, the fluid does no longer behave as an ideal gas (i.e., $Pv \neq RT$, whereas P is the gas pressure, v is the specific volume, R is the gas constant, and T is the temperature) and thermodynamics abides by very complex Equation of State (EoS). This behavior is typical of molecular complex compounds at conditions close to the liquid-vapor equilibrium, for pressures in the order of those corresponding to the critical point. Within this region, a single-phase fluid is also said to be in dense conditions, meaning that the gas dynamics of the flow significantly differs from its dilute-gas (ideal) counterpart. For instance, non-ideal phenomena include a decrease of the flow Mach number in supersonic

Declarations of interest: none

*Corresponding author: giulio.gori@inria.fr

expansions [11], the non-ideal evolution of the Mach number in diabatic supersonic nozzle flows [36] and the increase of the flow Mach number across oblique shock waves [17, 49]

The characterization of NICFD flows presents not only a theoretical interest, but it is also relevant to applications such as Organic Rankine Cycle (ORC), supercritical CO_2 power systems, turbogenerators, refrigerators and many others [9, 10, 51, 4]. Indeed, well-established and accurate thermodynamic models predict that several fluids currently employed in industrial processes feature non-ideal effects, with prominent examples being hydrocarbons, fluorocarbons, and siloxanes. Unfortunately, the gas-dynamic behavior of such substances is still unclear and, due to the inherent difficulties in running experiments, only a remarkably limited amount of experimental evidence is available up to date. Consequently, this shortage results into a lack of experimental data supporting theories and findings. In Ref. [8], the authors acknowledge an insufficient number of experimental results that forces the estimation of several fluid properties with ad hoc methods.

Since then, the community has been racing to overcome experimental issues and expand our knowledge about non-ideal fluid flows. The need to foster innovation in the NICFD field brought to the construction of a large number of experimental facilities. For instance, the Test-Rig for Organic VApors (TROVA) at Politecnico di Milano [40, 20] is a blow-down wind tunnel operating with molecular complex fluid vapors in the non-ideal regime. The Flexible Asymmetric Shock Tube (FAST) at TU Delft [26, 7] consists of a Ludwieg-tube to generate shock waves and to measure their velocity when propagating through organic vapors in a dense regime. Moreover, Delft University recently finalized the construction of the Organic Rankine Cycle Hybrid Integrated Device (ORCHID) [22], to investigate high-temperature supersonic flows and to test mini-ORC expanders. The Lappeenranta University of Technology is currently testing micro-ORC devices designed for the exploitation of waste heat from exhaust gases, in automotive applications. In particular, a micro-ORC test-rig devised to exploit waste heat from Diesel engine exhaust gases was recently built at the Laboratory of Fluid Dynamics [47, 46]. The ORC Ludwieg tube at Whittle Laboratory, University of Cambridge, is a facility designed to analyze the non-ideal flow across supersonic axial vane cascades, with a particular focus on the investigation of trailing edge effects [14]. The facility is designed to operate with several gases, including air, CO_2, and organic fluids. At the Münster University of Applied Sciences, the Closed Loop Organic Wind Tunnel (CLOWT), a closed-loop continuous-running wind tunnel, is currently under construction [32, 33]. The facility aims at investigating the flow around simple nozzle geometries, as well as turbine blade cascades, and it is designed to operate with fluoroketone Novec$^{\text{TM}}$ 649 ($CF_3CF_2C(O)CF(CF_3)_2$).

The offspring of experimental facilities for the investigation of non-ideal flows goes so far as to envision that a considerable amount of data will be soon available. This future calls for the development of numerical tools tailored to NICFD flow experiments, to take advantage of the collected data. Note that, in the field of NICFD, the vast majority of works published up to date consist in proofs of concept which rely on synthetic (numerically generated) data and not on measurements from real experiments. To mention a few, in [23] the authors propose a possible uncertainty-quantification based approach, to assess the accuracy of the thermophysical sub-model implemented in non-ideal CFD solvers. In [2], the authors aim at updating the epistemic uncertainty of ultrasonic flow meter measurements under non-ideal flow conditions through a Bayesian calibration of a computer model of the real process. Reference [27] proposed a Bayesian inference methodology to calibrate complex EoS used in numerical fluid flow solvers. Their work relies on synthetic aerodynamic data concerning a dense gas flow around a symmetric wing section.

Recently, experimental facilities started operating consistently and data are becoming available to the community. Reference [19, 16] presented the first-ever accuracy assessment of the complex thermodynamic fluid models for NICFD flows based on real experimental data. In particular, the referenced works take advantage of measurements concerning flows of siloxane MDM vapor in mildly non-ideal conditions.

In this work, we present the main steps to develop a Bayesian inference framework, and we provide an insight into the potential of experiments carried out using the TROVA test-rig at Politecnico di Milano. The long term goal is to develop a numerical tool to take advantage of the first-ever experimental campaign concerning flows expanding in the non-ideal regime [44, 42, 43, 41], to reduce the aleatoric and epistemic uncertainties inherent the thermodynamic fluid models. In particular, the Bayesian tool is developed to improve the estimation of the critical point coordinates and the value of the acentric factor of selected

compounds. To avoid dealing with measurement bias or epistemic uncertainties due to an approximated description of the actual test facility, we exploit synthetic data generated using the current state-of-the-art tools for NICFD. We present a framework tailored to experiments involving MDM (Octamethyltrisiloxane, $C_8H_{24}O_2Si_3$), but it is immediately extendable to any other compound (for instance MM hexamethyldisiloxane, $((CH_3)_3Si)_2O$). MDM is of the utmost importance for ORC applications because of its frequent use as working fluid in energy production plants powered by low-quality heat sources.

We consider three synthetic experiments in this work. Namely, two experiments aim at reproducing real tests carried out in the TROVA facility and involving flows expanding at either ideal or mildly non-ideal conditions. The third experiment is a virtual test designed to assess the Bayesian framework capabilities when dealing with flows in extreme non-ideal conditions. This latter experiment is yet to be attempted within the TROVA facility, and will probably require to substitute siloxane fluid MDM with a more thermally stable compound at the same reduced temperature, such as MM.

This paper is structured as follows: in Sec. 2 we introduce the non-ideal thermodynamics fundamentals, and we analyze the most relevant features characterizing NICFD fluid models. Sec. 3 describes the considered experiments, providing information about the TROVA facility and its the set up during the implementation of real tests. In particular, Sec. 3.3 describes the CFD model employed to generate the data and to build surrogates. Sec. 4 presents the Bayesian framework and, eventually, Sec. 5 reports the results obtained.

2. Thermodynamics

The definition of an appropriate fluid model is critical for achieving an accurate description of the thermodynamics of a system in the non-ideal regime. In the following, we briefly review the polytropic Ideal Gas (pIG), the polytropic Peng-Robinson (pPR) and the Span-Wagner (SW) fluid models. Hereinafter, a gas will be indicated as *polytropic* if the energy is a linear function of the temperature T for a large value of the specific volume i.e., if the specific heat at constant volume in the dilute gas limit is constant ($c_{v_\infty} = \text{const}$). For the sake of completeness, it is worth mentioning that a model for the specific heat law $c_{v_\infty}(T)$ could be obtained by polynomial fitting on experimental data or, for example, from the equipartition principle of classical statistical mechanics, see [3]. Nevertheless, we limit the ideal and the Peng-Robinson models to the polytropic gas assumption for simplicity. On the other hand, the SW model is a multiparameter EoS based on the Helmholtz potential, and it models the gas as non-polytropic one.

According to the state principle, which builds on top of the definition of a gas-dynamic fundamental relation [3], the local thermodynamic state of a system is determined by any two independent thermodynamic variables, provided that the chemical composition of the fluid does not change because of mixing or diffusion. Conveniently, the equations of state specifying the pressure P, the specific internal energy e and the specific entropy s can be expressed as a function of the fluid temperature T and specific volume v. Besides, the functional form of some EoS includes a set of material-dependent parameters that need to be estimated through experiments or via semi-empirical equations.

In this work, we aim at assessing the potential of TROVA experiments w.r.t. the calibration of the material-dependent parameter included in complex thermodynamics models for non-ideal flows. The final goal is to improve the accuracy of computational tools devised for renewable energy applications. In particular, we will attempt to estimate the temperature and pressure values at the critical point (T_{cr} and P_{cr}) and the acentric factor ω, a parameter that depends on the molecular structure of the fluid, of the siloxane MDM compound. Note that the state principle requires one to pledge the utmost attention in choosing the variables subject to inference. For instance, attempting to infer the critical density ρ_c together with P_{cr} and T_{cr} would result into an useless effort since the fluid model depends on two independent state variables only. Fixing any of these three parameters, if possible, would just reduce the number of degrees of freedom or, most likely, lead to thermodynamic inconsistencies. Note also that, according to the principle of corresponding states, it is possible to reformulate any EoS w.r.t. the reduced state variables i.e., state variables normalized w.r.t. the critical properties, so to obtain an adimensional formulation which is independent from the critical point coordinates. Nevertheless, such formulation is not suitable for the purposes expressed in this work since, for consistency, the calibration procedure would also require to scale the rough experimental data w.r.t. the critical (uncertain) coefficients.

2.1. The Polytropic Ideal Gas law

The polytropic Ideal Gas (pIG) law is one of the simplest models ever devised to describe the behavior of a fluid in the gaseous phase. The EoS for pressure, energy and entropy in the polytropic *Ideal Gas* model (pIG) read

$$P\left(T,v\right)=\frac{RT}{v}, \tag{1a}$$

$$e\left(T,v\right)=\frac{R}{\gamma-1}T, \tag{1b}$$

$$s\left(T,v\right)=\frac{R}{\gamma-1}\ln T+R\ln v, \tag{1c}$$

with R being the gas constant whereas γ is the specific heat ratio. The pIG model relies upon a set of assumptions which are reasonable for the vast majority of fluids, at least in a large portion of the thermodynamic state space. Nevertheless, as the state of a NICFD fluid approaches the saturation curve in the vicinity of the critical point i.e., the non-ideal region, the hypotheses underlying the pIG model fail. Consequently, the model loses accuracy.

2.1.1. The Polytropic Peng-Robinson Fluid Model

The polytropic Peng-Robinson (pPR) fluid model [29] is still relatively simple, yet it predicts the behavior of a gas, including non-ideal features, with a reasonable level of accuracy. The model includes a limited number of material-dependent parameters namely, the fluid critical temperature and pressure (T_{cr} and P_{cr}), the acentric factor ω, the covolume b and the magnitude of the van der Waals force a. The coefficients a and b provide a non-negligible contribution in the non-ideal regime and they are defined as

$$a=0.45724\frac{\left(RT_{\mathrm{cr}}\right)^{2}}{P_{\mathrm{cr}}}\qquad\text{and}\qquad b=0.0778\frac{RT_{\mathrm{cr}}}{P_{\mathrm{cr}}}. \tag{2}$$

The pPR EoS for pressure, energy and entropy read

$$P\left(T,v\right)=\frac{RT}{v-b}-\frac{a\alpha^{2}\left(T,\omega\right)}{v^{2}+2bv-b^{2}}, \tag{3a}$$

$$e\left(T,v\right)=\frac{RT}{\gamma-1}-\frac{a\alpha\left(T,\omega\right)\left(k+1\right)}{b\sqrt{2}}\tanh^{-1}\frac{b\sqrt{2}}{v+b}, \tag{3b}$$

$$s\left(T,v\right)=\frac{RT}{\gamma-1}lnT+R\ln\left(v-b\right)-\frac{a\alpha\left(T,\omega\right)k}{b\sqrt{2TT_{\mathrm{cr}}}}\tanh^{-1}\frac{b\sqrt{2}}{v+b}, \tag{3c}$$

where $\alpha\left(T,\omega\right)$ is a function that further models the inter-molecular interaction as a force depending on the temperature T. The $\alpha\left(T\right)$ function reads

$$\alpha\left(T,\omega\right)=\left[1+k\left(1-\sqrt{\frac{T}{T_{\mathrm{cr}}}}\right)\right], \tag{4}$$

where $k=0.37464+1.54226\omega-0.26992\omega^{2}$.

2.1.2. The Span-Wagner Fluid Model

The Span-Wagner (SW) EoS [37, 38] currently embodies the state-of-the-art for siloxane fluids [8]. Note that, in this work, we rely on the SW model for the generation of high-fidelity data only. The basis of the fluid model is the decomposition of the Helmholtz energy Ψ into two contributions. Namely, one contribution models the ideal gas behavior (Ψ^{ig}) whereas the other one accounts for the influence of inter-molecular forces (Ψ^{r}). The reduced form of the Helmholtz energy reads

$$\frac{\Psi\left(\tau,\delta\right)}{RT}=\frac{\Psi^{ig}\left(T,\rho\right)+\Psi^{r}\left(T,\rho\right)}{RT}, \tag{5}$$

τ being the reduced temperature ($T/T_{\rm cr}$) and δ the reduced density ($\rho/\rho_{\rm cr}$). The correction term Ψ^r consists in a multi-parameter functional form reading

$$\Psi^r(\tau,\delta) = n_1\delta\tau^{0.250} + n_2\delta\tau^{1.125} + n_3\delta\tau^{1.500} + n_4\delta^2\tau^{1.375} + n_5\delta^3\tau^{0.250} + n_6\delta^7\tau^{0.875} + n_7\delta^2\tau^{0.625}e^{-\delta} \quad (6a)$$

$$+ n_8\delta^5\tau^{1.750}e^{-\delta} + n_9\delta\tau^{3.625}e^{-\delta^2} + n_{10}\delta^4\tau^{3.625}e^{-\delta^2} + n_{11}\delta^3\tau^{14.5}e^{-\delta^3} + n_{12}\delta^4\tau^{12.0}e^{-\delta^3}, \quad (6b)$$

where $n_1,\ldots,n_{12}$ are 12 material-dependent parameters defined through sophisticated optimization algorithms that take advantage of data sets concerning fluids belonging to a certain family. As stated in Ref. [8], the SW functional form allows predicting the thermodynamic properties of the fluid within the experimental uncertainty. Therefore, any fluid model developed upon the SW functional form can serve as reference EoS. Note that, up to date, all published works concerning the optimization of the SW parameters rely on data sets related to static experiments only. Data considered in this work include flow measurements relative to expanding supersonic flows of siloxane compounds in the non-ideal regime. The fact that data are collected in an experiment involving a flow characterized by specific dynamics could potentially lead to different findings.

Compared to the pPR fluid model, the SW equations are far superior with regard to the achieved accuracy. In particular, the SW model has a higher performance in the critical region and close to saturation curve, yielding a reasonable description of the caloric properties. Such improvement is not only due to the relaxation of the polytropic assumption, which is a strong limit of the pPR model considered here, but also to the higher complexity which allows for more flexibility. In other words, in the close proximity of the critical point, the SW model performs far better than even the non-polytropic formulation of the Peng-Robinson EoS. Moreover, the SW model also proved better performances in extrapolating properties for which no data were available. For instance, basic properties such as pressure, fugacity, and enthalpy, can be extrapolated up to the limits of the chemical stability of the compound.

3. Synthetic vapor flow experiments

3.1. Model of experimental facility

In order to assess the feasibility of learning thermodynamics from vapor flow measurements, we need first to decide the type of flows and measurements that will be available for the Bayesian inference. Of course, it is essential to consider situations that can lead to actual physical implementation. To this end, we decided to consider the case of the TROVA test-rig [40, 20] at the Politecnico di Milano laboratory for Compressible-fluid dynamics for Renewable Energy Applications (CREA laboratory). This facility was designed to operate with different fluids, but we shall consider a specific one, namely, MDM [6], which is a siloxane compound.

In the TROVA facility, the fluid is vaporized in a high-pressure vessel equipped with electrothermal coils; when the desired conditions of pressure and temperature are obtained, a valve is opened, and the vapor flows through the test section depicted in Fig. 1(a-b) (the flow direction is from left to right), where probes and sensors are mounted. Different nozzle profiles can be assembled in the test chamber to produce the desired expansion rate. The TROVA is a blow-down facility and, as such, the operating conditions upstream the test-section change continuously in time as the high-pressure reservoir empties. Nevertheless, the conditions change rather slowly, and we shall assume steady upstream conditions during the expansion flow simulations. The latter approximation is supported by experimental observations which prove negligible flow unsteadiness over the considered time scale, see [44, 52].

In our synthetic experiments, we consider a unique profile consisting of the planar converging-diverging nozzle shown in Fig. 1(b). As the fluid flows through the nozzle, it undergoes an isentropic expansion and accelerates up to supersonic speed. The TROVA test section is equipped with static pressure probes mounted along the center-line at selected locations, indicated with black dots in Fig. 1(b). Temperature and pressure within the settling chamber are also monitored during the discharge. Moreover, the test section has an optical access to carry out schlieren measurements, such that the Mach number can be estimated from the experimental schlieren images, see [39, 44]. Practically, the Mach number can be estimated only

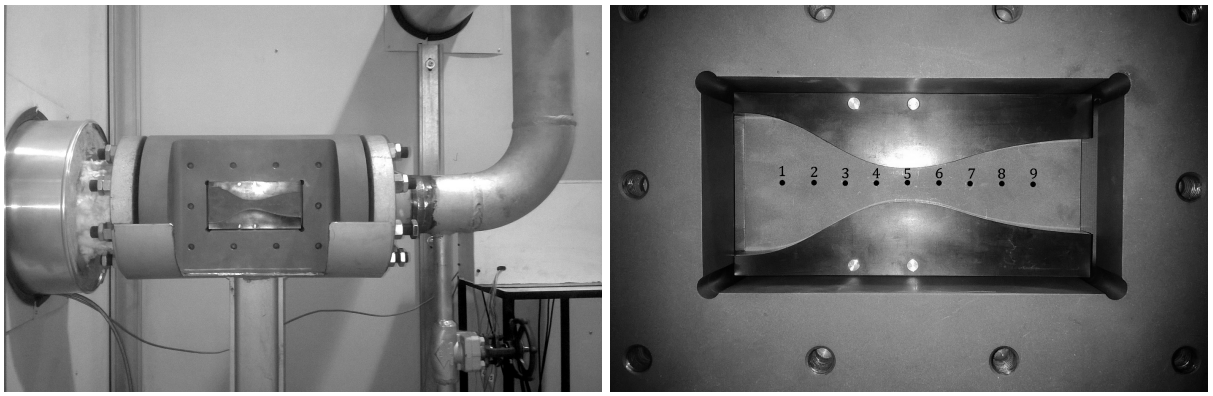

(a) (b)

Figure 1: The TROVA test section. The fluid flows from left to right. (a) Overview of the whole test section including the settling chamber, on the left side, and the pipeline directing the fluid into the discharge vacuum reservoir, on the right; (b) Enlargement of the converging-diverging nozzle mounted within the test section. Black dots show the locations where experimental pressure measurements are collected;

Exp.	P_{tot} [bar]	T_{tot} [K]	Z [-]
A	0.520	503	≈ 0.98
B	4.585	513	≈ 0.81
C	13.285	561.85	≈ 0.46

Table 1: Operating conditions (total pressure and temperature) and compressibility factor Z of the three expansion flows. The compressibility factor is evaluated at the inflow.

in the areas where the flow is supersonic. Nevertheless, in our synthetic experiments, we will virtually overstep this limitation and take advantage of Mach measures also in subsonic regions. Additionally, the flow velocity within the test section can be measured using a Laser Doppler Velocimetry (LDV) technique. Despite a preliminary investigation regarding the application of LDV to non-ideal flows [15], at the time of the writing real LDV measurements in the TROVA test-rig are being pursued and no published data is available. Nevertheless, we shall consider flow velocity measurements in our synthetic experimental settings in order to assess the impact of this information on the Bayesian learning procedure. Similarly, we shall use, in some of our synthetic experiments, static temperature data. Indeed, due to the boundary layer developing on walls, direct static temperature measurements in compressible flows could only be obtained using a device traveling at the fluid velocity without disturbing the flow [35]. Moreover, the test section walls are heated to prevent condensation during the discharge thus requiring a particular thermal insulation of thermocouples. This approach is rather unrealistic and, generally, static temperature measurements are obtained indirectly. In our analysis, all these issues are ignored and synthetic data are exploited to assess the intrinsic potential of temperature measurements.

3.2. The synthetic experiments

We consider three different experiments to assess the learning procedure. Namely, the experiments correspond to a quasi-ideal expansion (A); a mildly non-ideal expansion (B); and a highly non-ideal expansion (C) achieved at a relatively high reduced temperature. Table 1 reports the operating conditions i.e., the values of total pressure and total temperature at the inlet of the nozzle for the three expansions. Note that the operating conditions for Expansion C must be enforced with higher precision, because these conditions are close to the liquid-vapor saturation curve.

Expansions A and B could be practically achieved in real experiments within the TROVA test-rig. In contrast, Expansion C would not be achievable with MDM in the TROVA facility. Indeed, the high

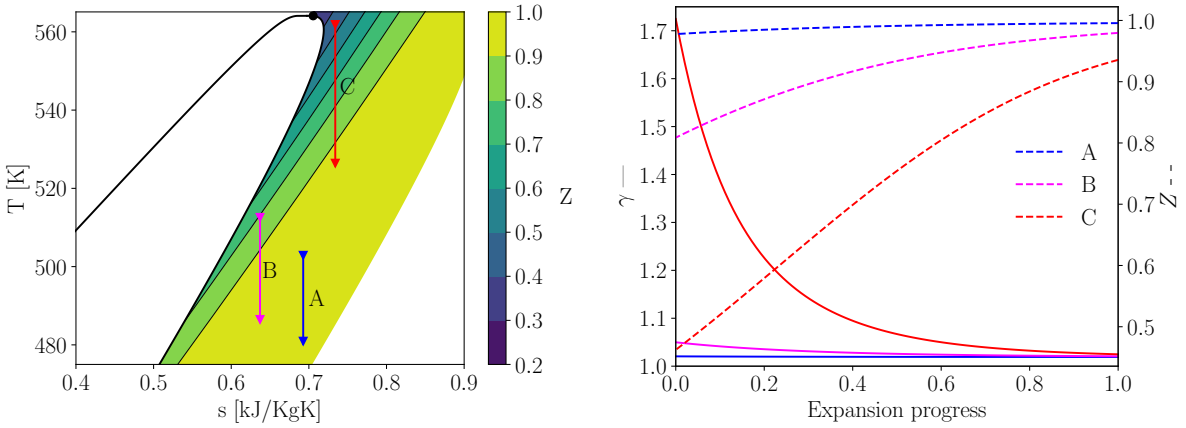

(a) (b)

Figure 2: (a) MDM T-s diagram showing the liquid-vapor saturation curve complemented by contours of the compressibility factory Z. The three isentropic expansions (A, B, C) are also reported. (b) Isentropic evolutions of the specific heat ratio γ (continuous line and scale on the left ordinate) and of the compressibility factor Z (dashed line and scale on the right ordinate) as functions of the expansion progress.

temperature required to reach this regime (see below) would perturb the chemical stability of the MDM compound. Possibly, similar expanding conditions may be achieved using a more stable fluid (e.g., siloxane MM).

Figure 2(a) reports the T-s (Temperature-Entropy) diagram of MDM in the vapor domain. This diagram was generated using the SW EoS. At the top of the vapor-liquid equilibrium curve, the black dot figures the fluid critical point. Contours provide the iso-values of the compressibility factor $Z \doteq Pv/RT$ within the thermodynamic state space. Given that for an ideal fluid $Z^{id} = 1$, the compressibility factor Z quantifies the deviation of thermodynamics w.r.t. the ideal behavior. In Fig. 2(a), we also report the three isentropic expansions (A, B and C) corresponding to the synthetic experiments. Expension A takes place in a region of the thermodynamic state space characterized by an approximately constant value of $Z \approx 1$, confirming that Expansion A is representative of an ideal flow. On the other hand, Expansion B originates in a region where $Z \approx 0.8$, a mildly non-ideal regime, and ends in the quasi-ideal portion of the T-s plane. Finally, Expansion C takes (almost entirely) place in the non-ideal region with values ranging from ≈ 0.48 to ≈ 0.95. Note that the Expansion C originates in the vicinity of the critical point, where the high temperature challenges the actual feasibility of this expansion.

The evolutions of Z along the expansions are easier to appreciate in Fig. 2(b), where they are reported as functions of the expansion progress *i.e.*, the temperature along the isentrope, using the dashed lines (scale on the right ordinate). Figure 2(b) also reports the dependence with the expansion progress of the specific heat ratio γ (continuous curves and scale on the left ordinate). As clear from Fig. 2(b), the polytropic gas assumption is reasonable for both expansions A and B, but it is arguably failing for Expansion C, where we appreciate a significant variation of γ from the inlet to the outlet of the nozzle.

3.3. Synthetic data generation

3.3.1. Synthetic data

The experimental conditions being set, and the measured quantities having been discussed, we now turn to the generation of the synthetic data for the Bayesian inference. These synthetic data come from numerical simulations of the expansions obtained using the SU2 open-source CFD solver (see details below in Section 3.3.2). The thermodynamic library embedded in SU2 implements both the pIG and the pPR models. The external library FluidProp [5] implements the latest SW model tailored to MDM, recently proposed in [45]. From now on, we refer to solutions based on the SW EoS as high-fidelity solutions. However, we

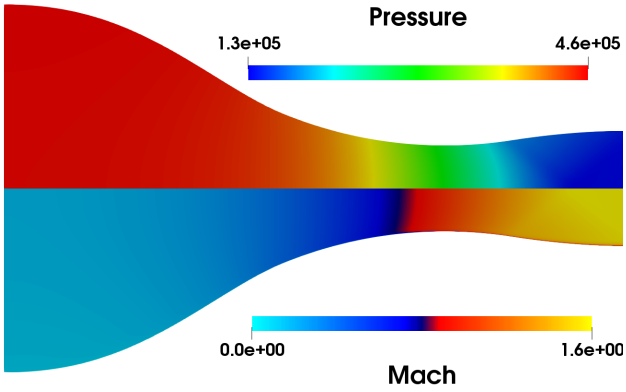

Figure 3: Pressure (upper half) and the Mach number (lower half) fields for a high-fidelity simulation of Expansion B.

consider synthetic data obtained with different models to test the inference process and assess the impact of model errors. That is, we attempt to calibrate the fluid flow parameters i.e., inlet total conditions, critical coordinates, acentric factor and specific heat ratio, by taking advantage (in independent runs) of synthetic measurements produced using models of different fidelity.

As an illustration of a simulation, Fig. 3 reports the pressure (on the upper side) and the Mach number (on the lower side) fields of the high-fidelity solution in the case of Expansion B. This solution varies smoothly and monotonically across the nozzle, underlying the mild non-ideal regime, with only quantitative differences compared to the ideal solution (not shown). Qualitatively, the flow retains an ideal behavior. For the two other expansions, A and C, all flow quantities also evolve smoothly within the domain, although non-ideal effects are more pronounced in the highly non-ideal Expansion C.

From the numerical solution of a given expansion and using a specific EoS, we generate the corresponding synthetic data by extracting the computed static pressures P_s, static temperatures T_s, Mach numbers M and flow speeds $\|\mathbf{v}\|$ at four locations along the nozzle centerline: $x_1 = 0.015$ [m], $x_2 = 0.045$ [m], $x_3 = 0.075$ [m] and $x_4 = 0.105$ [m]. In particular, the Mach number and flow speed measurements allows for an indirect evaluation of the speed of sound c through the well known relation $c = \mathbf{v}/M$. For a comprehensive description of the geometry of the nozzle and of the inflow conditions relative to this particular experiment we refer the reader to Sec. 3.3.2 or, for even more details, to Ref. [52]. Note that utmost attention shall be pledged in choosing the quantities subject to measure. Indeed, recall that the state principle dictates the dependency of the whole flow thermodynamic state upon two independent variables only. According to it, one should make sure that the measured quantities allow for a consistent characterization of the flow state. That is, using pressure, density and temperature measurements all at once would over specify the problem. The corresponding data set, unavoidably polluted by measurement noise, would prevent the convergence of the calibration procedure since thermodynamic consistency would never be met, possibly leading to non physical results. Synthetic data are generated using different thermodynamic models (pIG, pPR, SW). For each model, one has to prescribe the value of its parameters to perform the simulation. For consistency of the synthetic data, we used the same reference values reported in Tab. 2. These values were taken from [45], which also provides the values we use for the remaining SW model coefficients.

Quantity	P_cr [bar]	T_cr [K]	ω [-]	γ [-]
value	14.375	536.36	0.524	1.0183

Table 2: Reference values used in the synthetic data generation using the pIG and pPR models.

Table 3 reports the synthetic data, for the different combinations of expansions (A, B and C) and EoS (pIG, pPR and SW) used subsequently. Note that, in the calibration process, synthetic data are

	Location	A	B		C	
		pIG	pPR	SW	pPR	SW
P_s [bar]	x_1	0.515	4.528	4.527	13.172	13.178
	x_2	0.500	4.416	4.416	12.949	12.964
	x_3	0.403	3.629	3.627	11.143	11.976
	x_4	0.178	1.658	1.658	5.411	5.378
T_s [K]	x_1	502.7	512.4	512.4	561.4	561.4
	x_2	502.5	512.0	512.0	560.6	560.6
	x_3	500.5	509.4	509.2	554.7	554.3
	x_4	493.2	500.4	499.9	539.6	538.6
M [-]	x_1	0.169	0.177	0.176	0.208	0.210
	x_2	0.289	0.302	0.302	0.352	0.356
	x_3	0.714	0.729	0.728	0.776	0.784
	x_4	1.461	1.428	1.429	1.357	1.353
$\|\mathbf{v}\|$ [m/s]	x_1	22.6	19.3	19.4	12.5	12.0
	x_2	38.8	33.2	33.4	21.9	21.0
	x_3	95.6	83.4	83.9	60.1	58.7
	x_4	194.1	178.1	179.0	152.9	154.0

Table 3: Synthetic data for the three expansions and EoS.

artificially polluted with a random measurement error modeled as an unbiased Gaussian distribution with a variance proportional to the measured value. A comparison of the synthetic observations from the three expansions helps highlighting the differences among the considered fluid models. Differences arise because of the structural limitations characterizing the form of the (simpler) pIG and pPR fluid models. To a different extent, these limitations prevent simpler models from returning accurate predictions as the regime of the flow becomes more and more non-ideal. For instance, in a fully ideal regime, the absolute value of the Mach number across a converging-diverging nozzle only depends on the cross-sectional area distribution along the centerline (given that the nozzle is operating at the design point or in the under expanded regime). Therefore, simulations with the pIG model will always predict the very same local Mach values for all expansions *A*-*C* inflow condition. On contrast, the Mach predictions for the pPR and the SW models differ from the ideal ones and present a dependency on the upstream conditions in the NICFD regime, as shown is Tab. 3. Observing the synthetic data for the highly non-ideal expansion (C), we can also appreciate that the pPR and the SW models do yield different values for almost all the considered quantities (in particular pressure and flow velocity), despite the identical inflow conditions. The differences are small in the vicinity of the inlet (up to 0.04% for P_s and 0.2% for M) and increase as the flow expands along the nozzle (up to 6.9% for P_s and 1% for M). These discrepancies are due to the structural differences in the two models, in particular the restrictive polytropic gas assumption underlying the pPR model, and are the emphasized by the highly non-ideal regime of expansion C (the two EoS produce very similar predictions for expansion B). We shall take advantage of the flexibility provided by the synthetic data generated by exchangeable models to assess the impact of structural model error on the learning of thermodynamics model parameters.

3.3.2. CFD solver

In this section, we briefly describe the SU2 open-source CFD suite [13, 50, 30, 19, 18] used to simulate numerically the non-ideal expansions. As mentioned previously, the solver allows the selection of the pIG, pPR, and SW models. Thanks to the aerodynamic shape of the nozzle and to the relatively large Reynolds number of the flow (about $2\,10^6$ based on the flow conditions at the throat and on a reference length $l = 0.0084$ [m], the throat semi-height), CFD simulations rely upon the inviscid and adiabatic flow assumption. For all expansions, the nozzle is operating at design conditions so that flow gradients are smooth and no

detachments appear within the test section. Indeed, the flow consists of an isentropic stream in a domain with gentle geometrical variations. Viscous effects are limited to the boundary layer and they do not affect the inviscid core where we extract the synthetic data. The inviscid approximation was validated numerically in several earlier works for the same geometry and flow conditions, see [19, 16, 52]. These works confirm that, along the nozzle center line, the solution is almost insensitive to the presence of the thin boundary layer developing at the walls. The only noticeable viscous effect, though very limited, is found in the vicinity of the discharge section. However, this part of the domain contains no synthetic data point. Also, following previous simulation results reported in the referenced works, we exploit the symmetry of the nozzle to discretize only half of the domain using an unstructured grid of triangular elements containing 10,000 nodes.

In all simulations, the steady solution is obtained using an (implicit) time-marching method. A generalized Approximate Riemann solver of Roe type with a Monotone Upstream-centered Scheme for Conservation Laws (MUSCL) approximates the fluxes [48]. Second-order spatial accuracy is modulated by the van Albada slope limiter, which facilitates numerical convergence by preventing and suppressing possible spurious transient waves. A three-level multi-grid hierarchical approach is implemented to accelerate the computation. We monitor the convergence to the steady state by measuring the steady residuals at each iteration. Specifically, we stop the iterations when a reduction from their initial values of at least seven orders of magnitude for density residual, and six orders of magnitude for the energy, is attained.

4. Bayesian inference

4.1. Bayesian Inference

In the present work, the Bayes rule is employed to infer the thermodynamic model parameters using non-ideal expansion flow observations (in fact, the synthetic data). The actual experimental conditions, namely the total pressure and temperature at the inflow, are subjected to uncertainties as they can not be accurately measured in practice. Therefore, they are treated as additional parameters to be inferred, called nuisance parameters. In the following, we denote $\mathbf{q}$ the vector of all quantities involved in the inference: the thermodynamic model and nuisance parameters. Depending on the experiment and the thermodynamic model considered, the parameter vector $\mathbf{q}$ will include the flow total pressure (P_{tot}) and temperature (T_{tot}), the specific heat ratio (γ), the critical pressure (P_{cr}) and temperature (T_{cr}) and acentric factor (ω).

Having a priori knowledge of the values that these parameters can take, in the form of the prior probability distribution $\mathcal{P}(\mathbf{q})$, the objective is to derive the posterior distribution of $\mathbf{q}$ using the available data on the expansion flow. To this end, we rely of the Bayes formula which writes

$$\mathcal{P}\left(\mathbf{q} \mid \mathbf{o}\right) = \frac{\mathcal{P}\left(\mathbf{o} \mid \mathbf{q}\right) \mathcal{P}\left(\mathbf{q}\right)}{\mathcal{P}\left(\mathbf{o}\right)}. \tag{7}$$

In (7), we have denoted $\mathbf{o}$ the vector of observations data involved in the Bayesian inference, $\mathcal{P}\left(\mathbf{q} \mid \mathbf{o}\right)$ the posterior density of the parameter $\mathbf{q}$, $\mathcal{P}(\mathbf{o})$ the probability density of the data (also called the evidence in the present context), and $\mathcal{P}\left(\mathbf{o} \mid \mathbf{q}\right)$ the so-called likelihood of the data. The value of the synthetic data gathered in the vector $\mathbf{o}$ change with the expansion considered (see Tab. 3). Also, the vector of data will have a variable length depending on the data collected in the experiments. We will adapt the measured quantities to assess different aspects of the inference procedure. The vector $\mathbf{o}$ includes at least the synthetic static pressure P_{s} at the four locations in the nozzle. As discussed in Section 3.1, the addition of other quantities in $\mathbf{o}$ (Mach number, static temperature, and velocity) will also be considered to assess the information they bring.

The definition of the posterior distribution in (7), involves the prior and likelihood that are now specified. Note that the explicit computation of the evidence is not necessary for the Metropolis-Hasting approach discussed below. Indeed, the evidence acts as a scaling constant normalizing the integral of the posterior distribution to 1. Since we are here interested in the parameters calibration only i.e., finding peaks in the posterior distributions, we can spare the effort of computing the evidence. Concerning the prior of $\mathbf{q}$, we decided to restrict ourselves to uniform distributions only. This type of prior requires to fix a (finite) range of possible values for each of the unknown parameters in $\mathbf{q}$ and disregards any correlation or dependence

between the parameters. In practice, the prior ranges are selected to encompass reference values found in the literature. For instance, the value of P_{cr} for MDM reported by [12] is 14.600 [bar] whereas it is 14.200 [bar] in [1], 14.150 [bar] in [25] and 14.375 [bar] in [45], that is more than 3% variation between authors. Thermodynamic stability criteria and physical limits are also accounted for when selecting the a priori ranges. The ranges used in the numerical experiments will be provided for each of the test cases of the next section. Note that the goal of this paper is to assess whether it is possible to infer the true value of the EoS material-dependent parameters based on the different type of measurements. Since our investigation relies upon synthetic data, the point is more to show the information brought by the diverse data, for this particular experiment, rather than inferring the exact physical value of the parameters. That is, we know for sure that the truth (a synthetic nominal reference) is included within the imposed bounds. In this perspective, and in addition to the mitigation of numerical instabilities that may arise, it is not required to consider extremely wide prior supports for the unknown quantities. Priors are just coherent to what is the current state-of-the-art and they cover (with some margin) the whole span of reference values provided in literature.

One advantage of using the uniform prior is that $\mathcal{P}(\mathbf{q})$ is constant or zero outside the a priori range Q. This fact implies that the posterior is proportional to the likelihood for $\mathbf{q} \in Q$ and vanishing for $\mathbf{q} \notin Q$:

$$\mathcal{P}\left(\mathbf{q} \mid \mathbf{o}\right) \propto \begin{cases} \mathcal{P}(\mathbf{o} \mid \mathbf{q}) & \mathbf{q} \in Q, \\ 0 & \mathbf{q} \notin Q. \end{cases} \tag{8}$$

Thus, it remains to discuss the likelihood. The likelihood is the probability to observe the synthetic data $\mathbf{o}$ in the expansion flow governed by the considered EoS with the parameter values in $\mathbf{q}$. We recall that $\mathbf{q}$ specifies both the inflow conditions (P_{tot} and T_{tot}) and the thermodynamic model parameters. Writing $\tilde{\mathbf{o}}(\mathbf{q})$ the model prediction of the data, we choose to express the likelihood as the product of Gaussian probability density functions:

$$\mathcal{P}(\mathbf{o} \mid \mathbf{q}) = \prod_i \frac{1}{\sqrt{2\pi\sigma_i^2}} \exp\left[-\frac{|o_i - \tilde{o}_i(q)|^2}{2\sigma_i^2}\right]. \tag{9}$$

In (9), we have denoted σ_i the typical error (standard deviation) on the i-th component o_i of $\mathbf{o}$. It is seen that this likelihood penalizes values of $\mathbf{q}$ that yield larger discrepancies between the synthetic data $\mathbf{o}$ and their prediction by the model $\tilde{\mathbf{o}}(\mathbf{q})$. The primary assumption underlying the product form of the likelihood in (9) concerns the independence of the error on each of the component of $\mathbf{o}$. Although synthetic data are expected to involve correlated discrepancies, the use of independent error model is justified in the case of experimental measurement noise and is therefore appropriate for our numerical experiments.

4.2. Posterior Sampling

We have now specified all the ingredients defining the posterior distribution of the parameters of the inference. Unfortunately, the likelihood (9) has no closed-form expression because the model predictions of the synthetic data, $\tilde{\mathbf{o}}(\mathbf{q})$, involve the resolution of a complex expansion flow simulations. This limitation prevents the analytical evaluation of the posterior, and we rely on a sampling method for its estimation. Markov Chain Monte Carlo (MCMC) methods are often used to draw samples from complex multi-dimensional distributions with a large number of dimensions. Among the different MCMC alternatives, we use in this work the Metropolis-Hastings (MH) algorithm [21] to generate a sequence of random samples from the posterior. The core idea of the MH algorithm is to construct a random Markovian sequence of values for $\mathbf{q}$. The sequence is made to converge in distribution to the target posterior through the introduction of a suitable acceptance-rejection rule. The MH rule compares the likelihoods at the current step $\mathbf{q}_i$ of the chain and at the proposed next step $\mathbf{q}^*$, to decide if the latter is accepted or rejected as the next step $\mathbf{q}_{i+1}$.

A considerable number of steps, typically hundreds of thousands, is necessary to produce sufficiently many samples representative of the whole distribution, such that $\tilde{\mathbf{o}}(\mathbf{q})$ must be computed for multiple values of $\mathbf{q}$. As each evaluation requires the resolution of the full CFD model, direct application of the MH algorithm is computationally prohibitive. To alleviate this computational burden and make the MH algorithm feasible, a surrogate of the mapping $\mathbf{q} \mapsto \tilde{\mathbf{o}}(\mathbf{q})$ can be employed in place of full CFD model resolutions. Here, a

non-intrusive Polynomial Chaos (PC) expansion [24, 31] is employed to construct a surrogate model of $\tilde{\mathbf{o}}(\mathbf{q})$. The PC expansion $\hat{\mathbf{o}}(\mathbf{q})$ of $\tilde{\mathbf{o}}$ corresponds to the orthogonal projection into the linear span of a finite set of orthonormal polynomials in the parameters, $\Psi_\alpha(\mathbf{q})$,

$$\tilde{\mathbf{o}}(\mathbf{q}) \approx \hat{\mathbf{o}}(\mathbf{q}) = \sum_\alpha \hat{\mathbf{o}}\Psi_\alpha(\mathbf{q}).$$

Since the polynomials are orthonormal, the projection coefficients $\hat{\mathbf{o}}_\alpha$ are expressed as

$$\hat{\mathbf{o}}_\alpha = \langle \tilde{\mathbf{o}}(\mathbf{q}), \Psi_\alpha(\mathbf{q}) \rangle = \int \tilde{\mathbf{o}}(\mathbf{q})\Psi_\alpha(\mathbf{q}) d\mathcal{P}(\mathbf{q}).$$

Reminding that the prior density of the parameter is uniform, the integral can be efficiently approximated via numerical quadratures involving a limited number of model evaluation. In this study, we rely on tensorized Gauss quadrature rules. In that case, the computational complexity of the PC construction depends entirely on the dimensionality of the vector $\mathbf{q}$ and the polynomial degree of the PC basis. Several numerical tests (not shown) were performed to select a polynomial order of the PC expansion that ensures an absolute error small enough to be negligible on the subsequent inference procedure. According to the analysis, Legendre polynomials of order 3 were selected. A detailed assessment of the PC surrogate accuracy can be found in [16].

5. Results

In this section, we apply the Bayesian inference procedure to the learning of the parameters. We separately carry-out the inference on the synthetic data associated with the three expansion flows in order to assess the importance of the flow regime and the impact of the measured quantities on the quality of the inference. All the tests presented hereafter assumes the same measurement errors with standard deviations σ_i in equation (9) reported in Tab. 4. Measurement uncertainty was selected to correspond to the expected precision of real experiments. The standard deviations are reported as percentages of the measurements, which are in turn reported in Tab. 1 and 3, except for the static temperature whose accuracy is 1 Kelvin.

Quantity	P_{tot}	T_{tot}	P_{s}	T_{s}	M	$\|\mathbf{v}\|$
σ_i	2%	2%	0.3%	1 [K]	5%	1%

Table 4: Definition of the standard deviations σ_i used in the likelihood (9). The standard deviations are reported as percentages of the corresponding measurements, or in absolute value in the case of the static temperature.

The posterior densities reported in the following are build on 500 000 MCMC samples, collected after a burn-in phase of a minimum of 100 000 steps. The burn-in phase is a preprocessing step required to ensure that the Markov chain lands in a high probability region, so that it is more representative of the distribution that is being sampled. Indeed, if the chain has a relatively short length, and it starts in a low probability region, it could lead to a poor approximation of the inferred variables. In all cases below, the MH algorithm exhibits proper chain mixing and fast autocorrelation decay. A classical Kernel Density Estimation (KDE) method (Parzen–Rosenblatt window, see [34, 28]) was subsequently used to estimate the marginal distributions of the parameters from the generated samples sets.

5.1. Expansion A

As mentioned in Sec. 2, the polytropic gas assumption is an approximation of a more complex dynamics that, in principle, could be modeled using classical statistical mechanics. Figure 2(b) shows that the polytropic flow assumption is reasonable for Expansion A since γ remains approximately constant through the expansion. The immediate objective is thus to assess whether it is possible to estimate γ from the Expansion A (an ideal expansion). Because the same fluid model is employed to generate the synthetic

data and to carry out the calibration procedure, the inference is free of structural model errors and the posterior knowledge of γ directly reflects the information contained in the synthetic data and the (negative) impact of the uncertainty in the experimental conditions (P_{tot} and T_{tot}). The prior ranges of the parameters $\mathbf{q} = (P_{\text{tot}}, T_{\text{tot}}, \gamma)$ are reported in Tab. 5. These ranges are centered on the values considered to generate the synthetic data.

	Operating Conditions		Model Parameter
	P_{tot} [bar]	T_{tot} [K]	γ [-]
Prior range	$0.522 \pm 2\%$	$502.88 \pm 2\%$	$1.018317 \pm 1\%$

Table 5: Expansion A. Prior ranges expressed as percentages of the nominal values.

5.1.1. Inference from pressure measurements

We first assume that only static pressure measurements are available for the inference, and use the synthetic data for P_{s} reported in Tab. 3 for the Expansion A. Figure 4 reports the posterior marginal distributions of P_{tot}, T_{tot} and γ resulting from the Bayesian inference. Figure 4(a) shows a quite sharp posterior for P_{tot}, with a clear Maximum a Posteriori (MAP) ${P_{\text{tot}}}^{\text{MAP}} = 0.524$ [bar], which differs only by 0.38% from the value used to generate the data (see Tab. 1). In contrast, the posterior of T_{tot} depicted in Fig. 4(b) remains completely uninformative, denoting that the pressure measurements do not improve the knowledge of the temperature T_{tot}. Finally, the posterior of γ plotted in Fig. 4(c) presents maximum at $\gamma^{\text{MAP}} = 1.0223$, with a difference of only 0.39% w.r.t. the reference value, but is not as sharp as the posterior of P_{tot}.

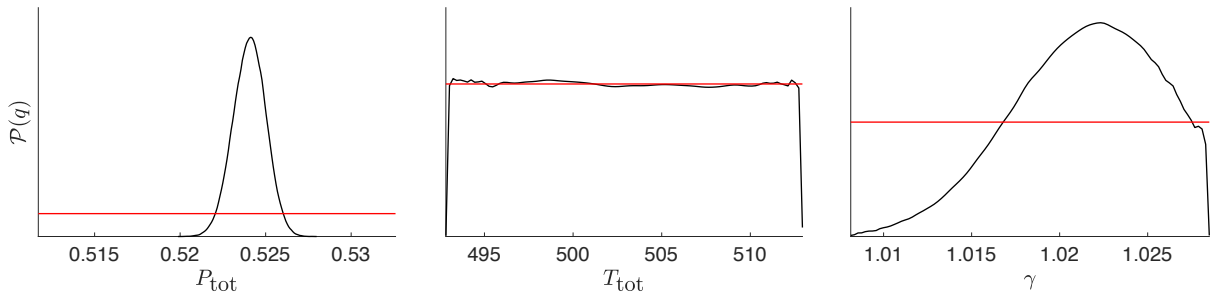

(a) P_{tot} posterior (b) T_{tot} posterior (c) γ posterior

Figure 4: Expansion A. Posterior marginal distributions using pressure measurements only. Priors are plotted in red, posteriors in black.

5.1.2. Inference from pressure, Mach and velocity measurements

In a second test for Expansion A, we repeat the previous inference considering now Mach and flow velocity measurements in addition to the pressure ones. We recall that these three quantities are measurable in the TROVA test-rig. Figures 5(a-c) report the resulting posterior distributions for P_{tot}, T_{tot},γ. Notably, the posteriors resemble the ones obtained using pressure measurements only, shown in Sec. 5.1.1. The T_{tot} posterior is still uninformative whereas ${P_{\text{tot}}}^{\text{MAP}}$ and γ^{MAP} fairly match the reference values. The inclusion of the Mach and velocity measurements does not improve the estimation of γ and the nuisance parameters noticeably. This limitation could be due to measurement uncertainty, but it was selected to correspond to the expected precision of real experiments.

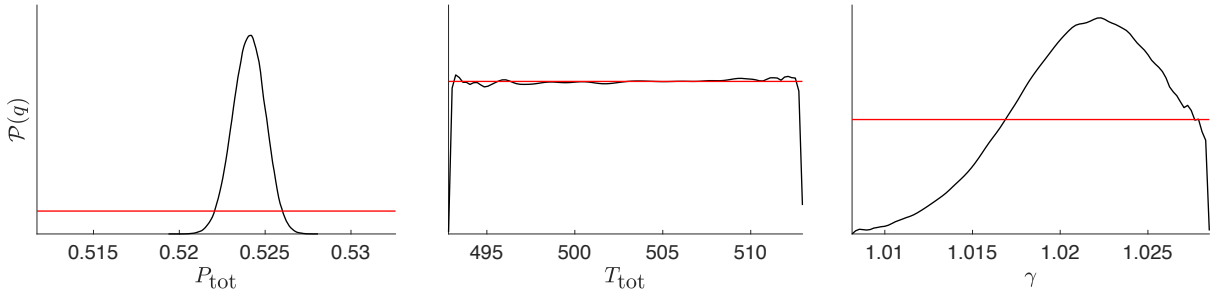

(a) P_{tot} posterior (b) T_{tot} posterior (c) γ posterior

Figure 5: Expansion A. Posterior marginal distributions using pressure, Mach, and velocity measurements. Priors are plotted in red, posteriors in black.

5.1.3. Inference from pressure and temperature measurements

Figures 6(a-c) report the posterior marginal distributions of P_{tot}, T_{tot}, γ, obtained considering static pressure and temperature measurements only. Contrary to the two previous cases, the inclusion of temperature measurements is seen to improve the posterior knowledge of T_{tot} and γ significantly. Notably, the error of the MAP values w.r.t the reference ones is of about 0.34%, 0.07% and 0.23% for P_{tot}, T_{tot} and γ, respectively. This improvement can be explained as follow. First, temperature measurements help to infer the total temperature of the flow better. Second, γ relates to the vibrational modes of the molecule and, therefore, it ultimately depends on the temperature of the gas. As a consequence, the learning of γ is positively impacted by the information gain on the temperatures.

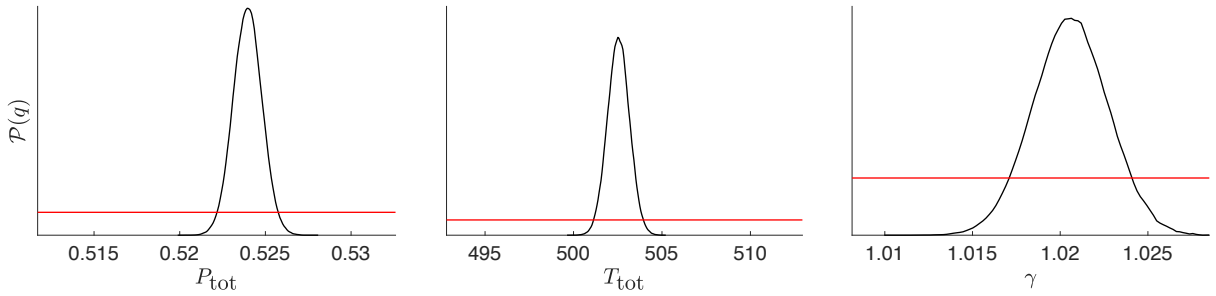

(a) P_{tot} posterior (b) T_{tot} posterior (c) γ posterior

Figure 6: Expansion A. Posterior marginal distributions using pressure and temperature measurements. Priors are plotted in red, posteriors in black.

5.1.4. Inference with known operating conditions

In the previous tests, we considered the expansion conditions P_{tot} and T_{tot} as uncertain and we included them in the inference process. To assess the impact of these uncertainties, we assume an exact knowledge of the inflow conditions and set P_{tot} and T_{tot} to the values used to generate the synthetic data. Therefore, it only remains to calibrate γ. Figure 7 reports the posterior distributions of γ obtained considering different measurements. Specifically, Fig. 7(a) reports the posterior considering static pressure measurements only, Fig. 7(b) uses pressure, Mach and velocity measurements, while Fig. 7(c) involves pressure and temperature measurements. The impact of perfectly knowing the flow conditions is evident when comparing these posteriors with their counterparts shown in the previous subsections: the inference of γ is significantly better with comparatively sharper densities. The values of γ_{MAP} are respectively 1.0157 (-0.25% from γ_{ref}),

1.0162 (-0.21%) and 1.0201 (0.18%). One can conclude from these results that, even for exactly known conditions, measurements of Mach and velocity are not much informative for inferring γ, while temperature measurements would be very beneficial.

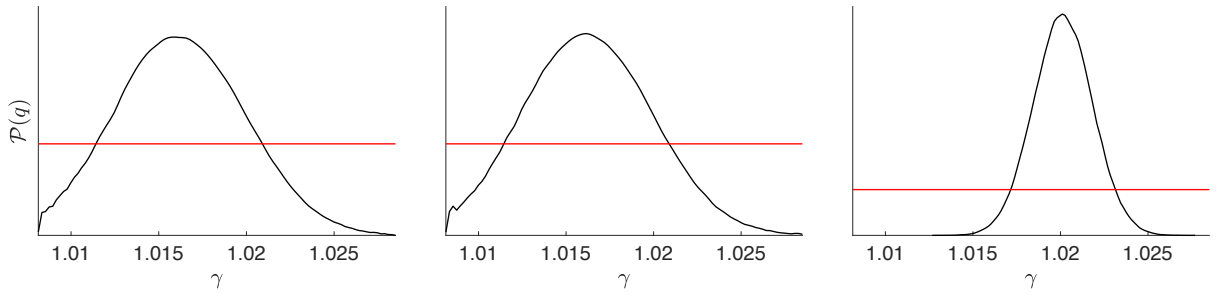

(a) Pressure only (b) Pressure Mach and velocity (c) Pressure and temperature

Figure 7: Expansion *A*. Posterior distributions of γ for perfectly known inflow conditions. Priors are plotted in red, posteriors in black.

5.2. Expansion B

Expansion *B* concerns the expansion of siloxane MDM vapor at mildly non-ideal conditions, see Fig. 2(b). We first assume uncertain inflow conditions (P_{tot} and T_{tot}), and calibrate the parameters of the pPR model (P_{cr}, T_{cr}, ω and γ) exploiting synthetic data generated using the same EoS (*i.e.*, avoiding model error). The posterior therefore involves six unknown parameters ($P_{\text{tot}}, T_{\text{tot}}, P_{\text{cr}}, T_{\text{cr}}, \omega, \gamma$). The priors are again uniform distributions with ranges reported in Tab. 6. Note that the priors ranges are not centered on the reference values used for the synthetic data and reported in Tab. 2.

	Operating Conditions		Model Parameter			
	P_{tot} [bar]	T_{tot} [K]	P_{cr} [kPa]	T_{cr} [K]	ω [-]	γ [-]
Prior range	4.586± 2%	512.56± 2%	1400± 5%	560± 3%	0.5± 70%	1.0183± 1.3%

Table 6: Expansion *B*. Priors ranges expressed as percentages of the nominal values.

5.2.1. A priori sensitivity analysis

Before presenting the inference results, we propose a brief a priori sensitivity analysis of the pressure through the expansion. Figure 8(a) shows the envelope of the expansion pressure profile. The envelope is estimated from the M samples used to construct the PC surrogate model. The pressure profile for the pPR model with the reference values is also reported in red. It is seen to fall well within the boundaries of the envelope. We exploit the PC surrogate to carry a sensitivity analysis to assess the importance of the individual parameters. Fig. 8(b) reports the evolutions through the expansion of the partial variances (part of the variance explained by the considered uncertain parameter) of the pressure when Fig. 8(c) focuses on the region around the nozzle discharge section. The profile of partial variances shows that the prior uncertainty on the total pressure P_{tot} utterly dominates the variability of the pressure profile, denoting that it is much less sensitive to variations of the other parameters (within the prior ranges). This dominance of the total pressure is raising serious questions about the possibility to calibrate the other parameters.

Figures 9(a), (b) and (c) report, respectively, the partial variances evolution of the Mach number, of the static temperature and of the flow speed. As clear from Fig. 9(a), overall the Mach number is poorly sensitive to any variation of the uncertain parameters. Indeed, the partial standard deviation is approximately equal to 0.0045 [-] at highest, 0.3% variability in terms of relative variation, in the close proximity of the discharge

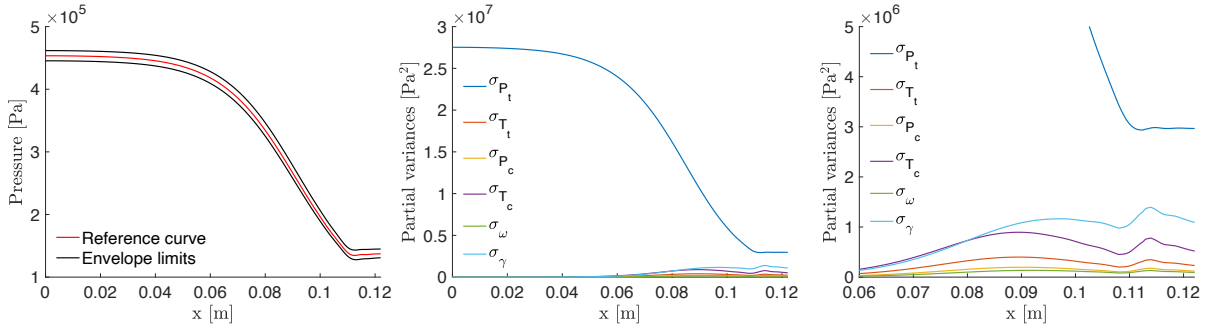

(a) Pressure profiles (b) Partial variances (c) Partial variances (close-view at nozzle)

Figure 8: Expansion B. Envelope of the pressure profiles and partial variances associated to the uncertain parameters.

region. This latter evidence suggests that Mach number measurements are expected to bring very little, if none, information into the inference process. Figure 9(b), reporting the static temperature partial variances, reveals instead a dominating role for the inlet total temperature uncertainty. At the discharge section, the specific heat ratio uncertainty gains relevance since it significantly contributes to the overall variability. This is a confirmation that temperature measurements would be beneficial to the inference process, as data would help fixing the caloric part of the thermodynamic problem. Eventually, Fig. 9(c) reports the partial variances of the flow speed. Once again, the plot reveals that the domain region close to the nozzle discharge section is more sensitive to parameter uncertainty. In particular, the flow speed variability appears to be mostly related to the uncertainty affecting the operating conditions namely, the inlet total temperature, and, to a lesser extent, to the value of critical temperature.

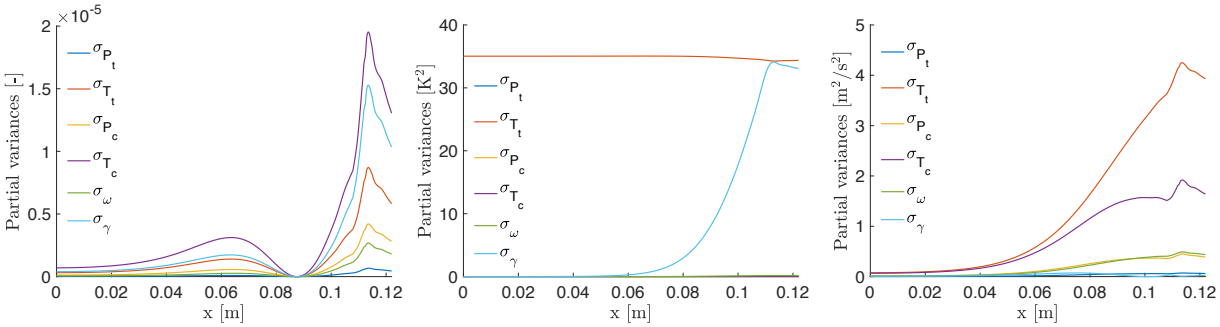

(a) Mach partial variances (b) Temperature partial variances (c) Flow speed partial variances

Figure 9: Expansion B. Mach, Temperature and flow speed partial variances associated to the uncertain parameters.

5.2.2. Inference from pressure measurements

We start by considering only static pressure measurements P_s for the inference. The posterior marginals of P_{tot}, T_{tot}, P_{cr}, T_{cr}, ω and γ are reported in Fig. 10. We see a poor gain for most of the parameters, except for P_{tot} and, to a lesser extent, γ. No noticeable improvement is reported concerning the knowledge of T_{tot}, P_{cr}, T_{cr} and ω, which have flat posterior marginals. This behavior is consistent with the sensitivity analysis of the pressure profile presented above. Note that the distance between ${P_{tot}}^{MAP}$ and the reference total pressure value is lower than 0.14%, when $\gamma^{MAP} = 1.0066$ with a difference of -1.15% w.r.t. its reference value.

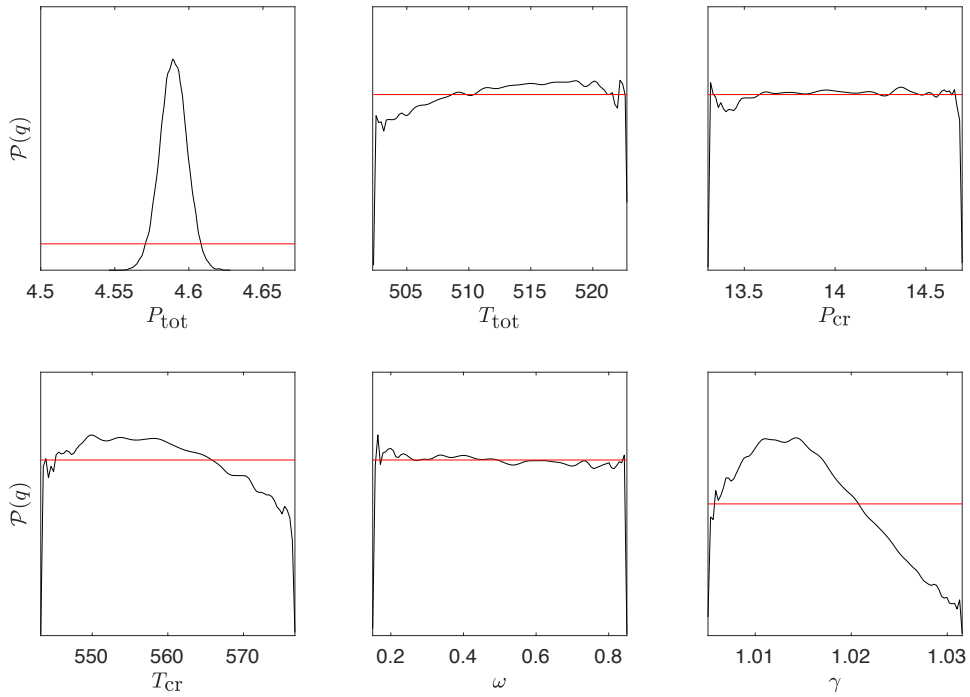

Figure 10: Expansion B. Parameters posterior marginal distributions using pressure measurements only. Priors are plotted in red, posteriors in black.

5.2.3. Inference from pressure, Mach and velocity measurements

Here, we investigate the effect of adding Mach and velocity measurements to the inference. Figure 11 shows the resulting posterior marginals. They reveal that the combination of the three measurements may be beneficial as it improves the inference of T_{tot}, T_{cr} and γ. Nevertheless, these posteriors are not sharp, and P_{cr} and the acentric factor ω remains very much uncertain a posteriori.

5.2.4. Inference from pressure and temperature measurements

Here, we consider the inference using pressure and temperature measurements. The resulting posterior marginals, reported in Fig. 12, reveal that the availability of temperature measurements would be very beneficial to the inference of the model parameters. In particular, the posterior marginals of T_{tot} and γ are much narrower than when using on pressure measurements. The γ^{MAP} is now equal to 1.0121, with a difference of -0.61 % w.r.t. the reference. However, the posteriors of P_{cr}, T_{cr} and ω remain poorly informative. Nevertheless, results confirm that temperature measurements would be very relevant to the calibrate complex fluid models.

5.2.5. Inference with fixed operating conditions

The a priori sensitivity analysis demonstrated that importance of the uncertain operating conditions, P_{tot} in particular, on the pressure variance. The relatively higher sensitivity of the pressure on P_{tot} explains why this parameter is better inferred than the others. In the following experiment, we again assumed perfect knowledge of the operating conditions, setting P_{tot} and T_{tot} to their reference values, and run the inference for the four parameters of PR model using the pressure measurements only. The resulting posterior marginals are reported in Fig. 13. Even if the dominating role of P_{tot} is inhibited, the posterior knowledge of the model parameters barely improves compared to the case where P_{tot} and T_{tot} are uncertain.

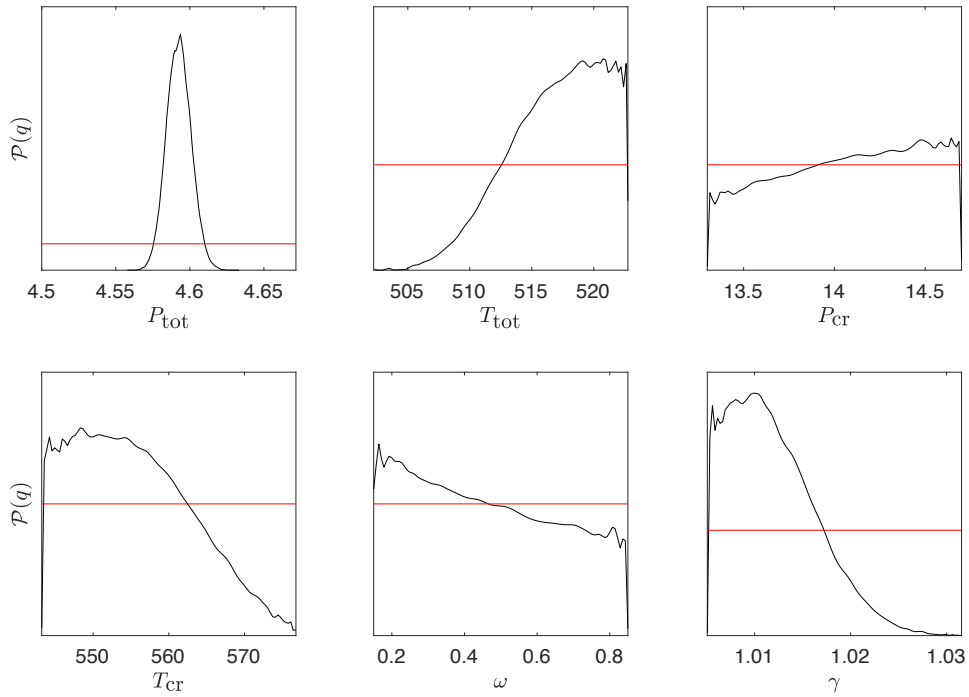

Figure 11: Expansion B. Posterior marginal distributions using pressure, Mach, and velocity measurements. Priors are plotted in red, posteriors in black.

When temperature measurements are also considered, the results presented in Fig. 14 indicates that γ is better known a posteriori, thanks to its strict relation with the caloric part of the problem. A more marginal improvement on T_{cr} is reported too. Nevertheless, overall results show that the combination of pressure and temperature measurements still did not lead to any significant improvement in the inferential process of P_{cr} and ω. The results presented in this section suggest that the considered expansion is not suitable for inferring all the parameters of the pPR fluid model correctly.

5.3. Expansion C

Expansion C is a virtual situation involving the expansion of siloxane MDM vapor at extremely non-ideal conditions, at pressure and temperature in the order of the critical ones, see Fig. 2(b). The reference inflow total conditions $P_{\mathrm{tot}} = 13.285$ [bar] and $T_{\mathrm{tot}} = 561.9$ [K] correspond to a compressibility factor $Z \approx 0.46$, see Tab. 1. This experiment would be not practically feasible with the MDM since the molecule would likely decompose at such high temperature, and a different fluid should be used in similar non-ideal conditions. Moreover, the variation of the heat specific ratio γ through the expansion, reported in Fig.2(b), reveals that the polytropic gas assumption fails in the considered conditions. Consequently, a polytropic gas model does not suit an expansion in such a regime. Nevertheless, relying on synthetic data, we can evaluate the potential of a virtual experiment in such extreme conditions and assess its suitability for the inference of the pPR model parameters. The objective here is to obtain fundamental information that will serve for the development of future experiments.

For this expansion, we neglect any uncertainty affecting the inflow conditions *i.e.*, the experimental conditions are perfectly controllable, and the inference reduces to the model parameters $\mathbf{q} = (P_{\mathrm{cr}}, T_{\mathrm{cr}}, \omega, \gamma)$. Moreover, given the very extreme thermodynamic conditions, a reduction of the priors of P_{cr} and T_{cr} was found necessary to ensure the numerical stability of the CFD solver over the whole initial uncertainty range. Indeed, variations of the pPR parameters affect the coordinates of the critical point and the shape of the

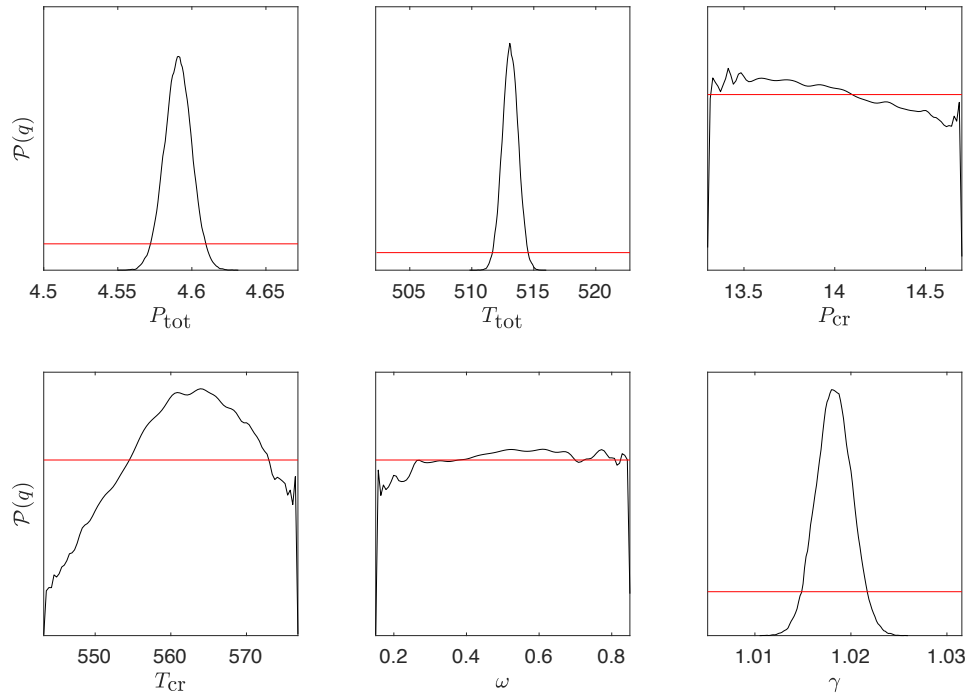

Figure 12: Expansion B. Posterior marginal distributions using pressure and temperature measurements. Priors are plotted in red, posteriors in black.

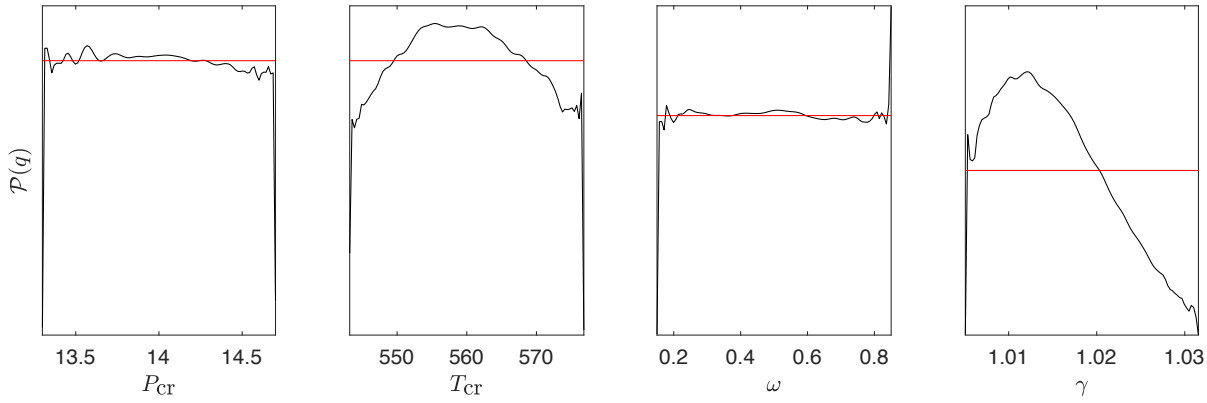

Figure 13: Expansion B. Posterior marginal distributions using pressure measurements only, in perfectly known operating conditions. Priors are plotted in red, posteriors in black.

liquid-vapor saturation curve. Since the expansion conditions considered are independent of the model parameter and chosen close to the critical conditions, too large variation ranges for the model parameters may cause the expansion to cross the liquid-water equilibrium curve, thus entering the two-phase region. In this situation, the CFD simulation can diverge or converge to a non-physical solution. Tab. 7 thus summarizes the prior ranges (assuming uniform distributions) for Expansion C.

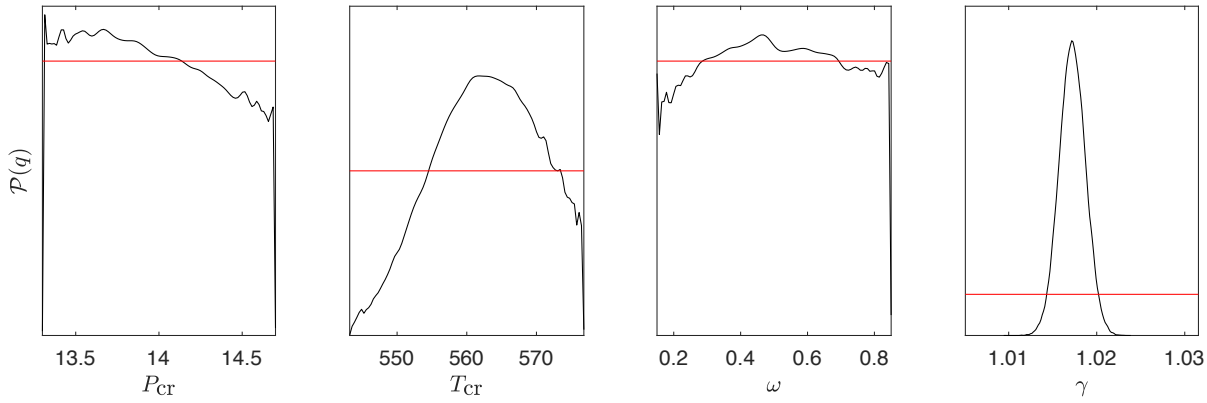

Figure 14: Expansion B. Posterior marginal distributions using pressure and temperature measurements, in perfectly known operating conditions. Priors are plotted in red, posteriors in black.

	Operating Conditions		Model Parameter			
	P_{tot} [bar]	T_{tot} [K]	P_{cr} [kPa]	T_{cr} [K]	ω [-]	γ [-]
Prior range	13.285	561.9	1430± 1%	564± 0.4%	0.5± 50%	1.0183± 1%

Table 7: Expansion C. Operating conditions and prior ranges for the model parameters.

5.3.1. Inference using polytropic Peng-Robinson based data

The inference algorithm is run first on synthetic data generated using the pPR model with the reference values. Although this model is expected to be physically inaccurate for the considered conditions, this experiment is carried out to get an insight on whether the highly non-ideal regime intrinsically allows for the inference of the critical point coordinates and acentric factor. Figure 15 reports the posterior marginals of the model parameters considering pressure measurements only. The posterior marginals are still covering the whole prior ranges. They do not concentrate much, although more than for the previous Expansion B, in particular for T_{cr} and ω. For all parameters, except perhaps P_{cr}, it is possible to extract a more likely subregion of the prior. This trend is an indication that the model starts to be sensitive to variations of the parameters in this highly non-ideal regime. The MAP values are $P_{\mathrm{cr}} = 14.374$ [bar], $T_{\mathrm{cr}} = 564.97$ [K], $\omega = 0.625$ [-] and $\gamma = 1.0180$ [-], with relative differences of -0.004%, -0.07%, 19.2% and -0.03%, respectively, to the reference values reported in Tab. 2.

As for the previous expansions, we also consider the inference using pressure and temperature measurements. Figure 16 presents the posterior marginals of the model parameters; once more, we see that γ significantly benefits from the temperature measurements. In contrast, the marginals of the other parameters do not show any significant improvement. The MAP values correspond to $P_{\mathrm{cr}} = 14.252$ [bar], $T_{\mathrm{cr}} = 563.8$ [K], $\omega = 0.639$ [-] and $\gamma = 1.0177$ [-] with a relative difference of 0.86%, -0.27%, 21.9% and -0.06%, respectively.

5.3.2. Inference using Span-Wagner based data

The state-of-the-art non-polytropic SW model is now employed to generate the synthetic data used as the measurements in the inference of the pPR model parameters. As mentioned, the polytropic gas-assumption fails in the conditions of the Expansion C. Therefore, the pPR model is not expected to be able to match the synthetic data based on a non-polytropic SW model. In other words, and contrary to the preceding examples, the inference involves some model error. This test case is then designed to assess whether it is possible to calibrate the pPR model, which is computationally way cheaper than the SW model, and to obtain accurate predictions.

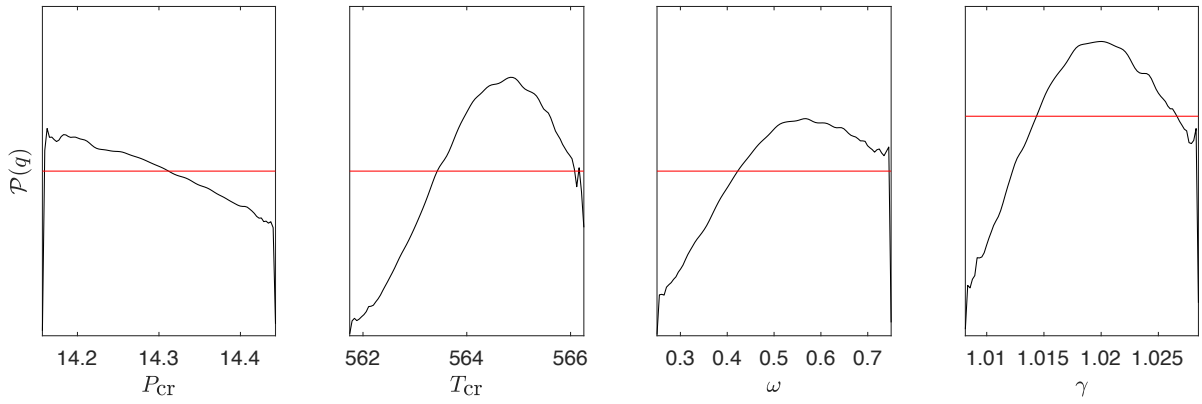

Figure 15: Expansion C. Posterior marginal distributions using pressure measurements generated with the pPR model. Priors are plotted in red, posteriors in black.

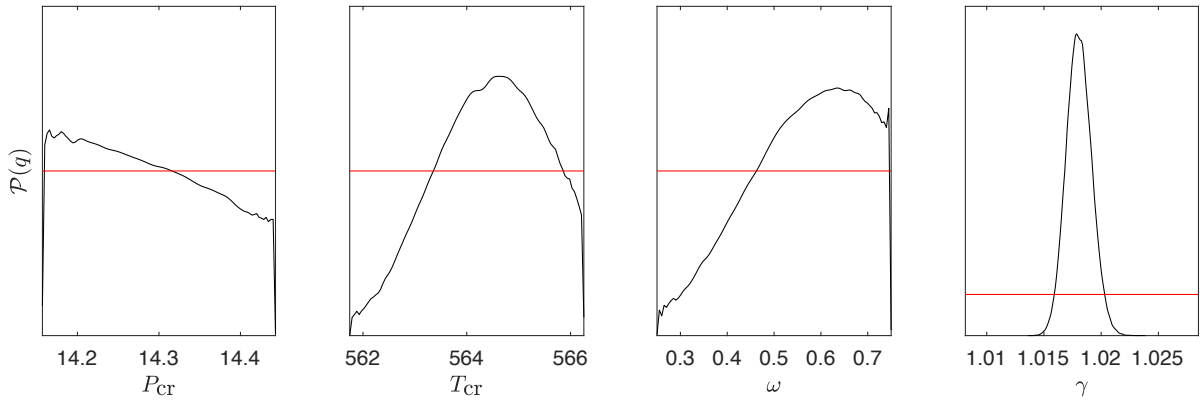

Figure 16: Expansion C. Posterior marginal distributions using pressure and temperature measurements generated with the pPR model. Priors are plotted in red, posteriors in black.

Figure 17 reports the posterior marginals considering pressure measurements only. Qualitatively, the information gained through the inference is comparable to the previous case using synthetic data from the pPR model (see Fig. 15). However, significant changes in the structure of the marginals are apparent for ω and γ, with a notable displacement of their MAP points. These differences in the MAP points highlight the differences in the synthetic data produced using the pPR and SW models. Similarly to the previous sections, Fig. 18 presents the posteriors obtained also considering the temperature measurements (based on the SW model). Once again, temperature measurements are seen to improve significantly the learning of γ whose posterior marginal is quite identical to the one for the pPR model synthetic data.

To complete the analysis of the model errors for Expansion C, we provide in Fig. 19 a comparison of the discrepancies between the two reference pressure profiles used to generate the synthetic data and their corresponding MAP predictions. Specifically, the pPR and SW reference solutions (using the parameters in Tab. 2) are compared with the pPR solutions for the MAP points found in Sect. 5.3.1 and 5.3.2 respectively. The differences are reported as local percentages relative to the reference solution, in the case of the inference using pressure Fig. 19(a), and pressure and temperature measurements Fig. 19(b). We first observe that the

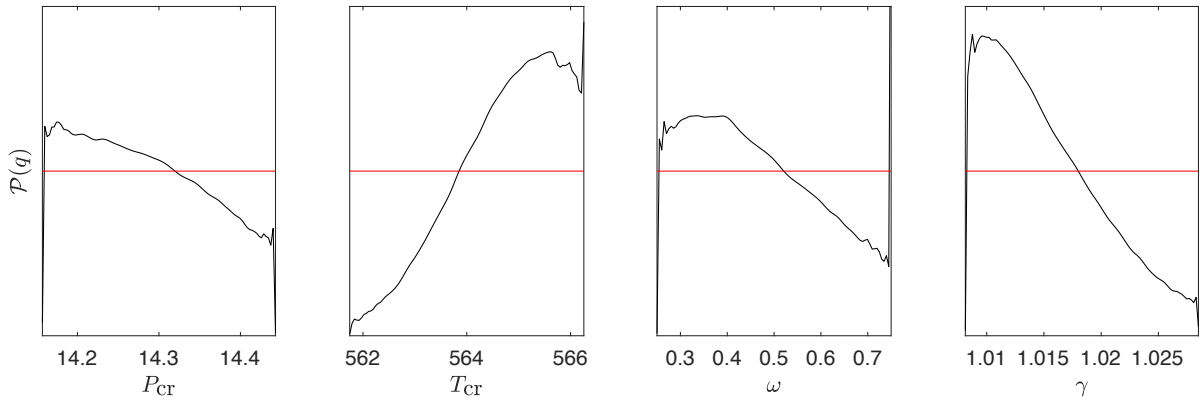

Figure 17: Expansion C. Posterior marginal distributions using pressure measurements only generated with the SW model. Priors are plotted in red, posteriors in black.

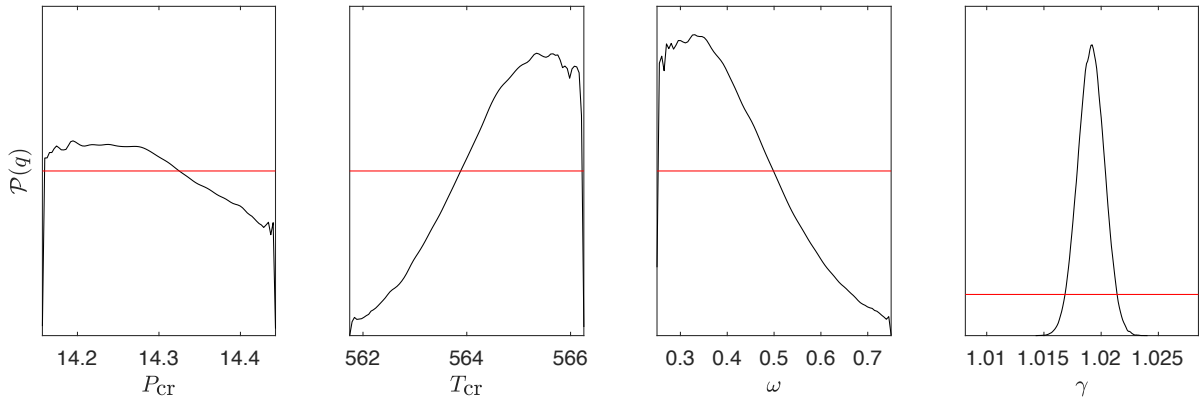

Figure 18: Expansion C. Posterior marginal distributions using pressure and temperature measurements generated with the SW model. Priors are plotted in red, posteriors in black.

magnitude of the relative differences are comparable when the inference involves model errors (synthetic data based on the SW model) or not (synthetic data based on the pPR model), suggesting that the differences between the two models are not too significant. Further, we recall that, in the absence of model error, the difference between the MAP solution and the reference one is only due to the noise in the measurements. One can observe that the relative difference is consistent with the standard deviation σ_i prescribed for the measurement accuracy (0.3%). The model error induced yields slightly higher relative differences, at the end of the expansion in particular, but the MAP pPR solution overall predicts the SW reference quite well. In addition, the plots show that if the introduction of temperature measurements in the inference improves the determination of γ in the two cases, its impacts on the MAP pressure profiles are small but distinct: the differences are seen to increase slightly in the case without model error, when they are barely affected in the case with model error. The low sensitivity on the specific heat ratio of the pressure profile explains these findings.

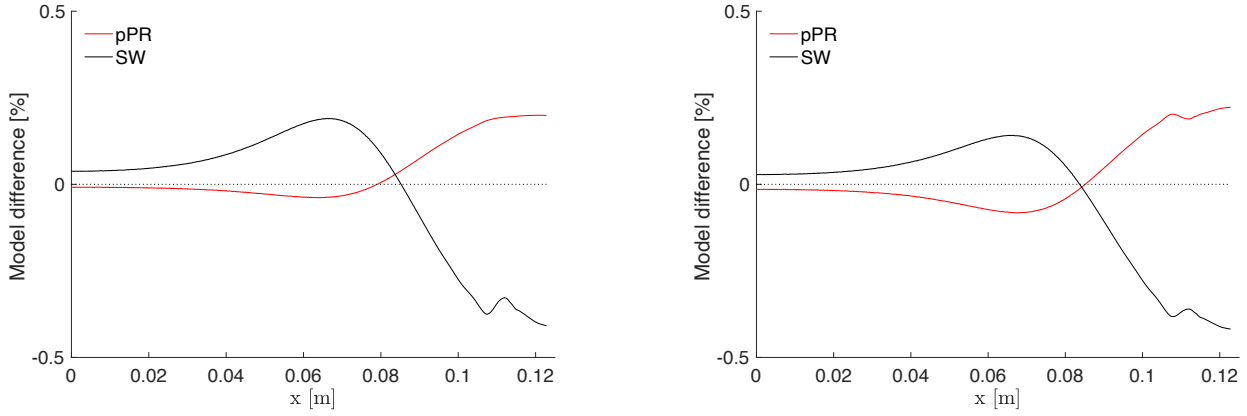

(a) Pressure measurements

(b) Pressure and temperature measurements

Figure 19: Expansion C. Relative differences in the pressure profiles between the reference and pPR MAP solutions, using pressure (left) or pressure and temperature measurements (right). The curves labeled pPR correspond to the inference using synthetic data based on the pPR model at reference values; the curve labeled SW correspond to the inference using synthetic data based on the SW model at reference values.

6. Conclusions

This work concerns the calibration of thermodynamic models for non-ideal fluids of interest in renewable energy applications. We investigate numerically the possibility of exploiting expansion flow measurements to infer the parameters of complex thermodynamic models for fluids exhibiting a non-ideal behavior. The TROVA test-rig at Politecnico di Milano serves as a model of the experimental facility, and we consider an isentropic flow of siloxane MDM vapor expanding through a planar converging-diverging nozzle. We considered several flow conditions ranging from ideal to highly non-ideal conditions. A Bayesian framework is employed to update the distribution of the model parameters using the flow measurements. The Bayesian framework accommodates uncertainties in the experimental conditions and the measurements. In practice, the measurements consist of synthetic data generated using numerical models. We followed a numerical approach with synthetic data because it allows investigating a) highly non-ideal experiments, that would be problematic to carry out in practice, b) the integration of quantities, such as temperature, not measured in existing facilities, and finally c) consider data with or without model error. It also prevents the presence of other sources of experimental errors such as geometrical uncertainties, uncertainties in sensor location, vapor composition and so on.

Overall, our results reveal the difficulty of learning thermodynamic model parameters from the expansion flow experiments as currently conducted in current facilities. The main reason is that the model predictions of the measurements, particularly the static pressure, are relatively sensitive to the flow conditions, while they do not depend much on the thermodynamic model parameters of interest. However, having a perfect knowledge of the flow conditions yields limited improvements. Similarly, velocity and Mach measurements were found to be quite uninformative while including temperature measurement helps inferring the experimental flow conditions and improves the posterior knowledge of the specific heat ratio γ. Further, the identification of both the acentric factor and specific heat ratio would require expansions in the vicinity of the saturation curve (highly non-ideal regime), conditions that would be very challenging to achieve in practice. Further, even if the model error is low, the experimental conditions precisely known and highly non-ideal, the critical pressure and temperature of MDM seem hard to determine.

Our numerical experiments allow drawing immediate recommendations for the improvement of existing experimental facilities and the design of future ones. First of all, to get the most from the measurements, we recommend improving the control or determination of the experimental conditions (P_{tot} and T_{tot}). Similarly, future experiments would gain from performing temperature measurements in the test section. In any

case, experimentalists should consider performing measurements in conditions that yield noticeable non-ideal effects, and so the sensitivity of the flow on the parameters of thermodynamic model is significant. Unfortunately, these conditions are likely to cause the decomposition of the fluid, thus questioning the practical feasibility for MDM siloxane. However, the inference for other fluids may be possible, such as for the more thermally stable compound siloxane MM. Future research efforts might be committed to develop new perspectives, helping thermodynamics modelers in choosing the appropriate EoS functional form based on the background information provided by the Bayesian framework presented here. To this extent, Bayesian model selection techniques or Bayesian model averaging might shed a new light on thermodynamics modeling.

Finally, our numerical framework can be used to design and assess the potential of different type of flows, besides the smooth expansions. In particular, it would be interesting to investigate the interest of different types of flow, for instance shock flows, that may be better suited to exhibit more sensitivity to the model parameters. Moreover, once potential experiments are selected, it would be necessary to assess their suitability to the inference of more advanced thermodynamic models and their robustness to possible geometrical uncertainties and model errors (possibly including the impact of turbulence model error).

Acknowledgements

This work was funded by the European Commission's H2020 program, through the UTOPIAE Marie Curie Innovative Training Network, H2020-MSCA-ITN-2016, Grant Agreement number 722734 and by the European Research Council under Grant ERC Consolidator 2013, project NSHOCK 617603.

References

[1] D. Ambrose. Vapor-liquid critical properties. *NPL Report Chem*, 107, 1980.

[2] Z. Belligoli, R.P. Dwight, G.J.P. Kok, and P. Lucas. A bayesian study of uncertainty in ultrasonic flow meters under non-ideal flow conditions. *Metrologia*, 54(4):584, 2017.

[3] H. B. Callen. *Thermodynamics and an introduction to thermostatistics*. Wiley, 2 edition, 1985.

[4] P. Colonna, E. Casati, C. Trapp, T. Mathijssen, J. Larjola, T. Turunen-Saaresti, and A. Uusitalo. Organic Rankine Cycle power systems: From the concept to current technology, applications, and an outlook to the future. *J. Eng. Gas Turb. Power*, 137(10), 2015.

[5] P. Colonna, T. P. der Stelt, and A. Guardone. FluidProp: A program for the estimation of thermophysical properties of fluids. Energy Technology Section, Delft University of Technology, The Netherlands, 2005.

[6] P. Colonna, A. Guardone, and N. R. Nannan. Siloxanes: a new class of candidate Bethe-Zel'dovich-Thompson fluids. *Phys. Fluids*, 19(10):086102–1–12, 2007.

[7] P. Colonna, A. Guardone, N. R. Nannan, and C. Zamfirescu. Design of the dense gas flexible asymmetric shock tube. *ASME Journal of Fluids Engineering*, 130, 2008.

[8] P. Colonna, N. R. Nannan, A. Guardone, and E. W. Lemmon. Multiparameter equations of state for selected siloxanes. *Fluid Phase Equilib.*, 244(2):193–211, 2006.

[9] P. Colonna, N.R. Nannan, and A. Guardone. Multiparameter equations of state for siloxanes: [(ch3)3-si-o1/2]2-[o-si-(ch3)2]i=1,. . . ,3, and [o-si-(ch3)2]6. *Fluid Phase Equilibria*, 263(2):115 – 130, 2008.

[10] P. Congedo, C. Corre, and P. Cinnella. Numerical investigation of dense-gas effects in turbomachinery. *Comput. & Fluids*, 49(1):290–301, 2011.

[11] M. S. Cramer and L. M. Best. Steady, isentropic flows of dense gases. *Phys. Fluids A*, 3(4):219–226, 1991.

[12] Eric Dickinson, Ian A. McLure, and Bernard H. Powell. Thermodynamics of n-alkane + dimethylsiloxane mixtures. Part 2.—vapour pressures and enthalpies of mixing. *J. Chem. Soc., Faraday Trans. 1*, 70:2321–2327, 1974.

[13] Thomas D. Economon, Dheevatsa Mudigere, Gaurav Bansal, Alexander Heinecke, Francisco Palacios, Jongsoo Park, Mikhail Smelyanskiy, Juan J. Alonso, and Pradeep Dubey. Performance optimizations for scalable implicit RANS calculations with SU2. *Computers & Fluids*, 129:146 – 158, 2016.

[14] F. J. Durá Galiana, A. P. S. Wheeler, J. Ong, and C. A. de M. Ventura. The effect of dense gas dynamics on loss in ORC transonic turbines. *Journal of Physics: Conference Series*, 821(1):012021, 2017.

[15] Simone Gallarini. Design and commissioning of a laser Doppler velocimetry seeding system for non-ideal fluid flows. Master's thesis, Politecnico di Milano, Italy, 2016.

[16] G. Gori. *Non-Ideal Compressible-Fluid Dynamics: Developing a Combined Perspective on Modeling, Numerics and Experiments*. PhD thesis, Politecnico di Milano, 2019.

[17] G. Gori, D. Vimercati, and A. Guardone. Non-ideal compressible-fluid effects in oblique shock waves. *Journal of Physics: Conference Series*, 821(1):012003, 2017.

[18] G. Gori, M. Zocca, G. Cammi, A. Spinelli, P.M. Congedo, and A. Guardone. Accuracy assessment of the non-ideal computational fluid dynamics model for siloxane mdm from the open-source su2 suite. *European Journal of Mechanics - B/Fluids*, 79:109 – 120, 2020.

[19] Giulio Gori, Marta Zocca, Giorgia Cammi, Andrea Spinelli, and Alberto Guardone. Experimental assessment of the open-source SU2 CFD suite for ORC applications. *Energy Procedia*, 129(Supplement C):256–263, 2017.
[20] A Guardone, A Spinelli, and V Dossena. Influence of molecular complexity on nozzle design for an organic vapor wind tunnel. *ASME J. Eng. Gas Turb. Power*, 135:042307, 2013.
[21] W. K. Hastings. Monte carlo sampling methods using markov chains and their applications. *Biometrika*, 57(1):97–109, 1970.
[22] A. J. Head, C. De Servi, E. Casati, M. Pini, and P. Colonna. Preliminary design of the ORCHID: a facility for studying non-ideal compressible fluid dynamics and testing ORC expanders. In *ASME Turbo Expo 2016*, number GT2016-56103, 2016.
[23] A.J. Head, S. Iyer, C. de Servi, and M. Pini. Towards the validation of a cfd solver for non-ideal compressible flows. *Energy Procedia*, 129:240 – 247, 2017. 4th International Seminar on ORC Power SystemsSeptember 13-15th, Milano, Italy.
[24] O. Le Maître and O. Knio. *Spectral Methods for Uncertainty Quantification*. Scientific Computation. Springer Netherlands, 1 edition, 2010.
[25] Daniel D. Lindley and Harry C. Hershey. The orthobaric region of octamethyltrisiloxane. *Fluid Phase Equilibria*, 55(1):109 – 124, 1990.
[26] T. Mathijssen, M. Gallo, E. Casati, N. R. Nannan, C. Zamfirescu, A. Guardone, and P. Colonna. The flexible asymmetric shock tube (FAST): a Ludwieg tube facility for wave propagation measurements in high-temperature vapours of organic fluids. *Exp. Fluids*, 56(10):1–12, 2015.
[27] X. Merle and P. Cinnella. Bayesian quantification of thermodynamic uncertainties in dense gas flows. *Reliability Engineering & System Safety*, 134(Supplement C):305 – 323, 2015.
[28] Emanuel Parzen. On estimation of a probability density function and mode. volume 33, pages 1065–1076, 1962.
[29] D. Y. Peng and D. B. Robinson. A new two-constant equation of state. *Ind. Eng. Chem. Fundam.*, 15:59–64, 1976.
[30] M. Pini, S. Vitale, P. Colonna, G. Gori, A. Guardone, T. Economon, J.J. Alonso, and F. Palacios. SU2: the open-source software for non-ideal compressible flows. volume 821, page 012013, 2017.
[31] M T Reagan, H N Najm, B J Debusschere, O P Le Maître, O M Knio, and R G Ghanem. Spectral stochastic uncertainty quantification in chemical systems. *Combustion Theory and Modelling*, 8(3):607–632, 2004.
[32] F. Reinker, K. Hasselmann, S. aus der Wiesche, and E. Y. Kenig. Thermodynamics and Fluid Mechanics of a Closed Blade Cascade Wind Tunnel for Organic Vapors. *Journal of Engineering for Gas Turbines and Power*, 138:052601, 2016.
[33] F. Reinker, E. Y. Kenig, M. Passmann, and S. aus der Wiesche. Closed Loop Organic Wind Tunnel (CLOWT): Design, Components and Control System. *Energy Procedia*, 129(Supplement C):200–207, 2017.
[34] Murray Rosenblatt. Remarks on some nonparametric estimates of a density function. volume 27, pages 833–837, 1956.
[35] Giuseppe P. Russo. 5 - temperature measurements. In Giuseppe P. Russo, editor, *Aerodynamic Measurements*, pages 143 – 160. Woodhead Publishing, 2011.
[36] G. H. Schnerr and P. Leidner. Diabatic supersonic flows of dense gases. *Phys. Fluids A*, 3(10):2445–2458, 1991.
[37] R. Span and W. Wagner. Equations of state for technical applications. I. Simultaneously optimized functional forms for nonpolar and polar fluids. *Int. J. Thermophys.*, 24(1):1–39, 2003.
[38] R. Span and W. Wagner. Equations of state for technical applications. II. Results for nonpolar fluids. *Int. J. Thermophys.*, 24(1):41–109, 2003.
[39] A. Spinelli, A. Guardone, F. Cozzi, M. Carmine, R. Cheli, M. Zocca, P. Gaetani, and V. Dossena. Experimental observation of non-ideal nozzle flow of siloxane vapor mdm. In *3rd International Seminar on ORC Power Systems, Brussels, Belgium, 12-14 October*, 2015.
[40] A Spinelli, M Pini, V Dossena, P Gaetani, and F Casella. Design, simulation, and construction of a test rig for organic vapours. *ASME J. Eng. Gas Turb. Power*, 135:042303, 2013.
[41] Andrea Spinelli, Giorgia Cammi, Simone Gallarini, Marta Zocca, Fabio Cozzi, Paolo Gaetani, Vincenzo Dossena, and Alberto Guardone. Experimental evidence of non-ideal compressible effects in expanding flow of a high molecular complexity vapour. *Experiments in Fluids*, 59(8):126, Jul 2018.
[42] Andrea Spinelli, Giorgia Cammi, Marta Zocca, Simone Gallarini, Fabio Cozzi, Paolo Gaetani, Vincenzo Dossena, and Alberto Guardone. Experimental observation of non-ideal expanding flows of siloxane MDM vapor for ORC applications. *Energy Procedia*, 129:1125 – 1132, 2017.
[43] Andrea Spinelli, Fabio Cozzi, Giorgia Cammi, Marta Zocca, Paolo Gaetani, Vincenzo Dossena, and Alberto Guardone. Preliminary characterization of an expanding flow of siloxane vapor mdm. *Journal of Physics: Conference Series*, 821(1):012022, 2017.
[44] Andrea Spinelli, Fabio Cozzi, Marta Zocca, Paolo Gaetani, Vincenzo Dossena, and Alberto Guardone. Experimental investigation of a non-ideal expansion flow of siloxane vapor MDM. In *Proceedings of the ASME 2016 Turbo Expo, Soul*, number GT2016-57357, 2016.
[45] Monika Thol, Frithjof H. Dubberke, Elmar Baumhögger, Jadran Vrabec, and Roland Span. Speed of sound measurements and fundamental equations of state for octamethyltrisiloxane and decamethyltetrasiloxane. *Journal of Chemical & Engineering Data*, 62(9):2633–2648, 2017.
[46] T. Turunen-Saaresti, A. Uusitalo, and J. Honkatukia. Design and testing of high temperature micro-ORC test stand using Siloxane as working fluid. *Journal of Physics: Conference Series*, 821(1):012024, 2017.
[47] A. Uusitalo, J. Honkatukia, and T. Turunen-Saaresti. Evaluation of a small-scale waste heat recovery organic Rankine cycle. *Applied Energy*, 192:146–158, 2017.
[48] Bram Van Leer. Towards the ultimate conservative difference scheme. v. a second-order sequel to Godunov's method. *Journal of computational Physics*, 32(1):101–136, 1979.
[49] Davide Vimercati, Giulio Gori, and Alberto Guardone. Non-ideal oblique shock waves. *Journal of Fluid Mechanics*,

847:266–285, 2018.

[50] Salvatore Vitale, Giulio Gori, Matteo Pini, Alberto Guardone, Thomas D Economon, Francisco Palacios, Juan J Alonso, and Piero Colonna. Extension of the SU2 open source CFD code to the simulation of turbulent flows of fluids modelled with complex thermophysical laws. In *22nd AIAA Computational Fluid Dynamics Conference*, number AIAA Paper 2760, 2015.

[51] A. Wheeler and J. Ong. The role of dense gas dynamics on organic rankine cycle turbine performance. *J. Eng. Gas Turbines Power*, 135(10):102603, 2013.

[52] M. Zocca. *Experimental observation of supersonic non-ideal compressible-fluid flows*. PhD thesis, Politecnico di Milano, 2018.